A thalamic reticular circuit for head direction cell tuning and spatial navigation

Authors: Gil Vantomme, Zita Rovó, Romain Cardis, Elidie Béard, Georgia Katsioudi, Angelo Guadagno, Virginie Perrenoud, Laura MJ Fernandez, Anita Lüthi*

*Lead contact

Affiliations: Department of Fundamental Neurosciences, University of Lausanne, Rue du Bugnon 9, 1005 Lausanne, Vaud, Switzerland

Summary

To navigate in space, an animal must refer to sensory cues to orient and move. Circuit and synaptic mechanisms that integrate cues with internal head-direction (HD) signals remain, however, unclear. We identify an excitatory synaptic projection from the presubiculum (PreS) and the multisensory-associative retrosplenial cortex (RSC) to the anterodorsal thalamic reticular nucleus (TRN), so far classically implied in gating sensory information flow. *In vitro*, projections to TRN involved AMPA/NMDA-type glutamate receptors that initiated TRN cell burst discharge and feedforward inhibition of anterior thalamic nuclei. *In vivo*, chemogenetic anterodorsal TRN inhibition modulated PreS/RSC-induced anterior thalamic firing dynamics, broadened the tuning of thalamic HD cells, and led to preferential use of allo- over egocentric search strategies in the Morris water maze. TRN-dependent thalamic inhibition is thus an integral part of limbic navigational circuits wherein it coordinates external sensory and internal HD signals to regulate the choice of search strategies during spatial navigation.

Keywords: Anterior thalamus; Retrosplenial cortex; Presubiculum; Allocentric; Egocentric; Synaptic inhibition; Burst discharge; Perseverance; Optogenetics; Chemogenetics

Correspondence: anita.luthi@unil.ch

Introduction

To reach a goal, search for food, or avoid a predator, navigation in space is essential. To do so accurately, animals rely on sensory landmarks in the environment to monitor and adapt their path and body orientation in space. Sensory cortices elaborate information they receive from the sensory organs, and they interact with widespread thalamo-cortico-hippocampal networks that contain internal representations of space and body orientation to guide navigation (Hinman et al., 2018; Vélez-Fort et al., 2018). In the interest of survival in a constantly changing world, salient environmental cues have to be integrated rapidly with spatial signals so that navigational strategies can be adapted prior to full cortical elaboration. Accordingly, important integrative steps enabling sensory guided spatial navigation may be engaged at subcortical levels (Hinman et al., 2018; Knudsen, 2018). A major site for subcortical gating of external sensory stimuli is the inhibitory thalamic reticular nucleus (TRN) that shows a unique anatomical positioning at the interface between sensory thalamic nuclei and cortex (Crabtree, 2018; Pinault, 2004; Scheibel and Scheibel, 1966). Activity in TRN controls the gain of sensory inputs (Le Masson et al., 2002), sharpens receptive fields in thalamic sensory nuclei (Lee et al., 1994; Soto-Sánchez et al., 2017), underlies sensory selection in divided attentional tasks (Ahrens et al., 2015; Wimmer et al., 2015), and is involved in sensory induced flight responses (Dong et al., 2019).

To date, the TRN has not been implied in the gating of spatial information. Lesion studies, however, suggest that TRN contributes to covertly directing a rat's self-orientation to the target stimulus, such that orienting movements can be rapidly executed (Weese et al., 1999). Moreover, anterior thalamic nuclei (ATN) are part of the brain's navigational system (Dumont and Taube, 2015), and there is anatomical evidence in rodent that anterodorsal TRN innervates ATN (Gonzalo-Ruiz and Lieberman, 1995a, b; Lozsádi, 1995; Pinault and Deschênes, 1998; Scheibel and Scheibel, 1966), although this has been questioned in cat (Paré et al., 1987). The anterodorsal (AD) thalamic nucleus, part of the ATN, contains a large proportion of HD cells tuned to the direction of the rodent's head in space (Taube, 1995). The HD signal is generated within dorsal tegmental and lateral mammillary nuclei based primarily on vestibular signals and is then relayed to AD and from there to PreS (Sharp et al., 2001a; Sharp et al., 2001b; Stackman and Taube, 1998). Although the TRN has been proposed to be part of HD circuits (Peyrache et al., 2019), the underlying functional anatomy remains elusive. Possible equivalences and differences to the canonical sensory TRN-thalamocortical circuits thus remain speculative. Here, we hypothesized that if the TRN is to mediate subcortical sensory gating effectively, it should serve as an entry point for information flow to ATN to control the processing of HD signals.

59 The anterior thalamic HD representation is updated rapidly, within < 100 ms by external visual
60 landmarks (Zugaro et al., 2003), to which direct input from the dorsal presubiculum (dPreS)
61 (Goodridge and Taube, 1997), indirect input from dPreS via the lateral mammillary nucleus (Yoder
62 et al., 2015) and the retrosplenial cortex (RSC) (Clark et al., 2010) are thought to contribute. Both
63 PreS and RSC are reciprocally connected (van Groen and Wyss, 1990) and receive afferents
64 from ATN, primary and secondary visual cortex, integrating information relevant for egocentric
65 and allocentric, external cue-guided, navigation (Clark et al., 2018; Dumont and Taube, 2015;
66 Mitchell et al., 2018; Simonnet and Fricker, 2018). Behaviorally, lesions of dPreS compromise
67 rapid orienting behaviors based on landmarks (Yoder et al., 2019), whereas RSC lesions lead to
68 multiple deficits in spatial navigation and memory formation (Clark et al., 2018; Mitchell et al.,
69 2018). Although there is evidence for a topographically organized cortical feedback from RSC to
70 rat and monkey anterodorsal TRN (Cornwall et al., 1990; Lozsádi, 1994; Zikopoulos and Barbas,
71 2007), the nature of this corticothalamic communication has never been characterized. Indeed,
72 current models of HD circuits involving ATN, dPreS and RSC (Dumont and Taube, 2015; Perry
73 and Mitchell, 2019; Peyrache et al., 2017; Simonnet and Fricker, 2018) and of the brain's 'limbic'
74 navigational system (Bubb et al., 2017) largely disregard a functionally integrated TRN. In spite
75 of this gap of knowledge, the notion of a 'limbic' anterior TRN has been proposed recently
76 (Halassa et al., 2014; Zikopoulos and Barbas, 2012).
77 In this study, we combined tracing techniques, *in vitro* and *in vivo* electrophysiological recordings
78 together with a spatial navigation task to probe the synaptic integration and the function of TRN
79 in the communication between PreS, RSC and ATN.
80

81 # Results

82 ## RSC and PreS send topographically organized projections to ATN and TRN

83 To determine afferent projections to the anterodorsal portion of the TRN, we injected small
84 volumes (50-100 nl) of red retrobeads into anterodorsal TRN of C57BL6/J mice (4-8-week-old)
85 and identified sites of red punctate fluorescent labeling 5 – 7 days later. Four out of 19 injections
86 were restricted to the dorsal portion of the anterior TRN, as verified by parvalbumin (PV)-
87 immunostaining (Fig. 1A1, Suppl. Fig. 1). The size of injection sites was comparable to previous
88 reports using nanobead injections in TRN (Antal et al., 2014). We inspected brain areas in which
89 punctate retrobead labeling was present and clearly separated from the bulk of beads around the
90 injection site. We found punctate staining in the adjacent AD, laterodorsal (LD) and in the
91 centrolateral (CL) nuclei of the thalamus (Fig. 1A2, identified in 3 out of 4 injections), consistent

with prior tracing studies (Gonzalo-Ruiz and Lieberman, 1995a, b; Lozsádi, 1995; Pinault and Deschênes, 1998). Labeling was also found in deep layers of prelimbic cortex that extended into infralimbic and cingulate, and, in two cases, into motor cortical areas (not shown), consistent again with a previous study in rat (Lozsádi, 1994). Our attention was drawn to a distinct stretch of puncta extending from parahippocampal regions into RSC that was present for all four injections (Fig. 1A2, Suppl. Fig. 1). Labeling included in particular the deep layers of the PreS that is interposed between the subiculum, the parasubiculum and the RSC (Ding, 2013; Simonnet and Fricker, 2018).

We next used the anterograde tracer, *Phaseolus vulgaris*-leucoagglutinin (PHAL-L), to further assess anatomical projections specifically from RSC and PreS to anterior TRN. Through a panel of injections (n = 20) that targeted restricted portions of RSC, dPreS and ventral PreS (vPreS) (Fig. 1B1), we noted a nucleus-specific labelling pattern in the LD, AD, and anteroventral (AV) thalamus (the later is also part of ATN) (Fig. 1B2). Injections centered within the RSC labeled large portions of AD and LD, while sparing AV, whereas PreS-centered injections covered more restricted portions of LD, AD and AV. vPreS injections labeled the most lateral portion of LD and AV. Using confocal microscopy to follow the path of PreS/RSC fibers on their way to ATN and LD (together referred as ATN+), we realized that these traversed the TRN as a bundle that showed marked arborizations within the most anterodorsal portion of TRN (Fig. 1B3). Arborizations surrounded the TRN somata in dense plexuses and ran along portions of dendrites, suggesting that they formed synaptic contacts.

The PreS/RSC establishes functional excitatory synapses onto TRN

To quantify these anatomical observations in terms of possible functional synapses, we used whole-cell patch-clamp recordings in acute coronal slices from brains of mice injected with AAV1-CaMKIIa-ChR2-EYFP into PreS/RSC 3 – 5 weeks earlier (Fig. 2A). Cells patched within anterodorsal TRN showed rebound burst behavior, as recognizable by repetitive high-frequency bursts of action potentials after brief hyperpolarization, similar to posterior sensory TRN cells (Fig. 2B) (Fernandez et al., 2018). Electrical properties were also comparable to those of their posterior counterparts that are innervated by the primary somatosensory cortex S1 (Fernandez et al., 2018; Vantomme et al., 2019), but cells produced less repetitive bursts (Fig. 2C). Cells in AD, AV and LD showed properties typical for dorsal thalamocortical neurons, notably the presence of only a single rebound burst discharge (Huguenard, 1996) (Suppl. Fig. 2).

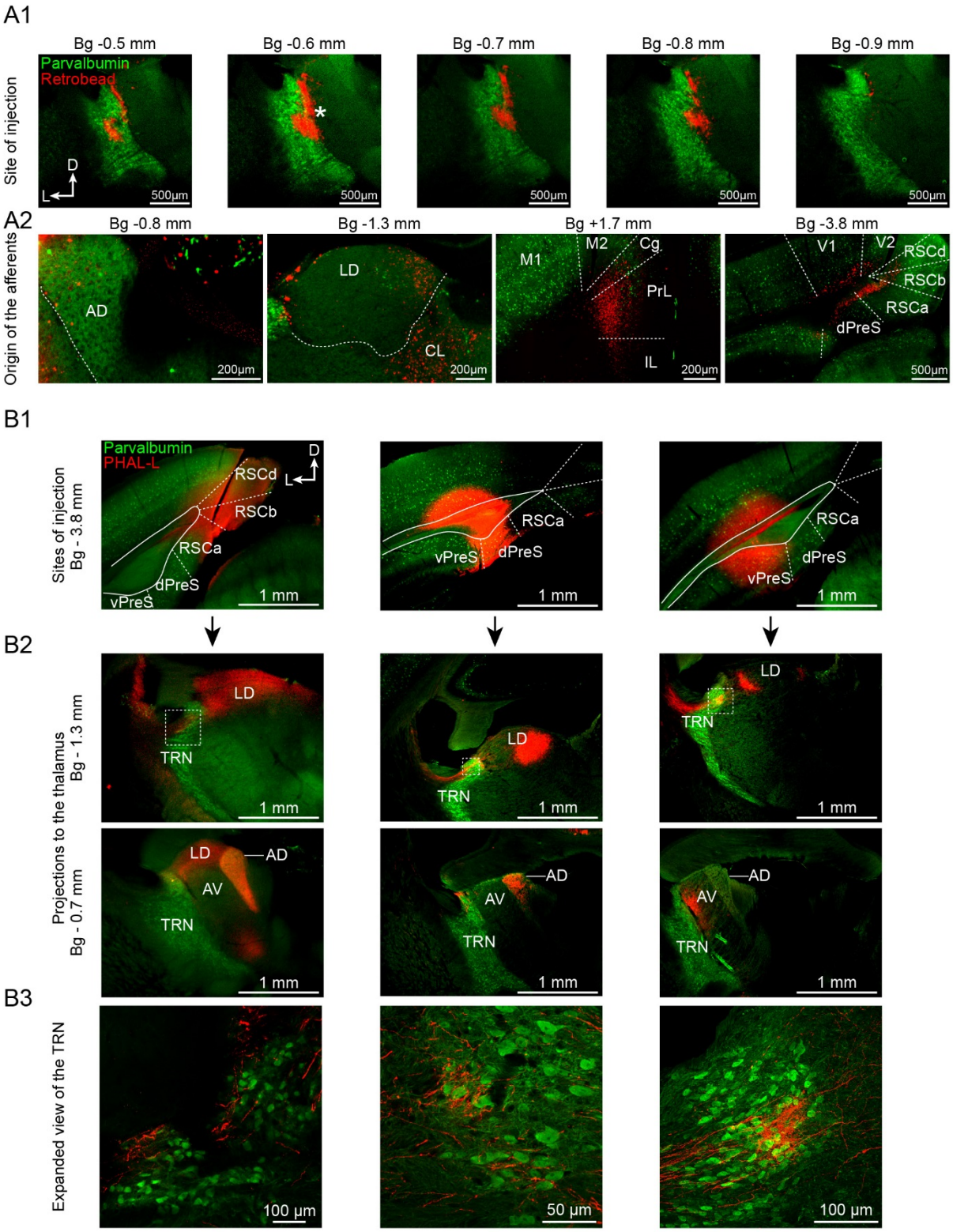
A1
Site of injection
Bg -0.5 mm
Bg -0.6 mm
Bg -0.7 mm
Bg -0.8 mm
Bg -0.9 mm
Parvalbumin
Retrobead
D
L
500µm
A2
Origin of the afferents
Bg -0.8 mm
Bg -1.3 mm
Bg +1.7 mm
Bg -3.8 mm
AD
LD
CL
M1
M2
Cg
PrL
IL
V1
V2
RSCd
RSCb
RSCa
dPreS
200µm
500µm
B1
Sites of injection
Bg - 3.8 mm
Parvalbumin
PHAL-L
vPreS
1 mm
B2
Projections to the thalamus
Bg - 1.3 mm
Bg - 0.7 mm
TRN
AV
B3
Expanded view of the TRN
100 µm
50 µm

126 **Figure 1. The RSC and the PreS send topographically organized projections to ATN and**
127 **TRN.**

128 **(A1)** Epifluorescent micrographs of mouse coronal brain sections showing a retrobead (red)
129 injection site (*) into the anterior portion of the TRN, which spread ~300 µm along the
130 anteroposterior extent of the TRN (immunostained for PV, green). Bg, Bregma. **(A2)**
131 Epifluorescent micrographs showing retrogradely labeled brain regions. Anterodorsal thalamus
132 (AD) – Laterodorsal thalamus (LD) – Centrolateral thalamus (CL) – Cingulate cortex (Cg) –
133 Prelimbic/Infralimbic cortex (PreL/IL) – dorsal Presubiculum (dPreS) – Retrosplenial cortex (RSC)
134 – Visual cortex (V1/V2) – Motor cortex (M1/M2). **(B1)** Epifluorescent micrographs of 3 different
135 injection sites of PHAL-L (red) into (from left to right) RSC, dPreS and ventral PreS (vPreS).
136 Green, PV+ neurons. **(B2)** Epifluorescent micrographs of coronal sections in ATN at Bg -1.3 mm
137 (top) and -0.7 mm (bottom). Note labeled fibers visible in the anterodorsal TRN (dotted squares).
138 **(B3)** Expanded confocal microscopy views of areas indicated by dotted squares in B2, AV,
139 anteroventral thalamus.

140

141 Optogenetic stimulation of PreS/RSC fibers was applied while recording from voltage-clamped
142 neurons of the anterodorsal TRN and of AD, AV and LD (Fig. 2D,E). The location of cells within
143 the different thalamic nuclei was evident while guiding the patch pipette to the target region and
144 was confirmed in a subgroup of cells through perfusion with neurobiotin and *post-hoc* recovery (n
145 = 33/106) (Fig. 2D1). Rapid synaptic inward currents were elicited in > 80 % of all recorded cells
146 for all areas (Fig. 2D2,D3). Synaptic currents were time-locked to the stimulus, with a fixed and
147 short latency to response onset and sub-millisecond jitter (Fig. 2D4,D5). Response latency was
148 inversely proportional to light intensity (Suppl. Fig. 2), which is consistent with an action potential-
149 dependent mode of synaptic transmission (Gjoni et al., 2018). There is thus a direct,
150 monosynaptic connection from PreS/RSC to anterodorsal TRN and to AD, AV and LD.

151 Light-evoked postsynaptic currents (EPSCs) were mediated by glutamatergic synaptic receptors,
152 as verified in a subset of 5 TRN and 5 neurons of AD, AV or LD (jointly referred to here as ATN+)
153 (Fig. 2E1). Thus, the AMPA receptor antagonist 6,7-Dinitroquinoxaline-2,3(1H,4H)-dione (DNQX,
154 40 µM, bath-application) reduced responses by > 90 % at -60 mV (Fig. 2E1,E2). The small
155 remaining current component was abolished by the NMDA receptor antagonist DL-2-Amino-5-
156 phosphonovaleric acid (APV, 100 µM, bath-application), as measured at +40 mV (Fig. 2E1, E2).
157 NMDA/AMPA ratios were comparable to previous studies on corticoreticular and corticothalamic
158 synapses in the sensory sectors of TRN (Fernandez et al., 2017). Moreover, the TRN-EPSCs had
159 a twice-shorter half-width than ATN+-EPSCs (Fig. 2E3) and a faster decay time (Fig. 2E4).
160 PreS/RSC inputs thus convey a phasic excitatory input onto anterodorsal TRN cells.

161

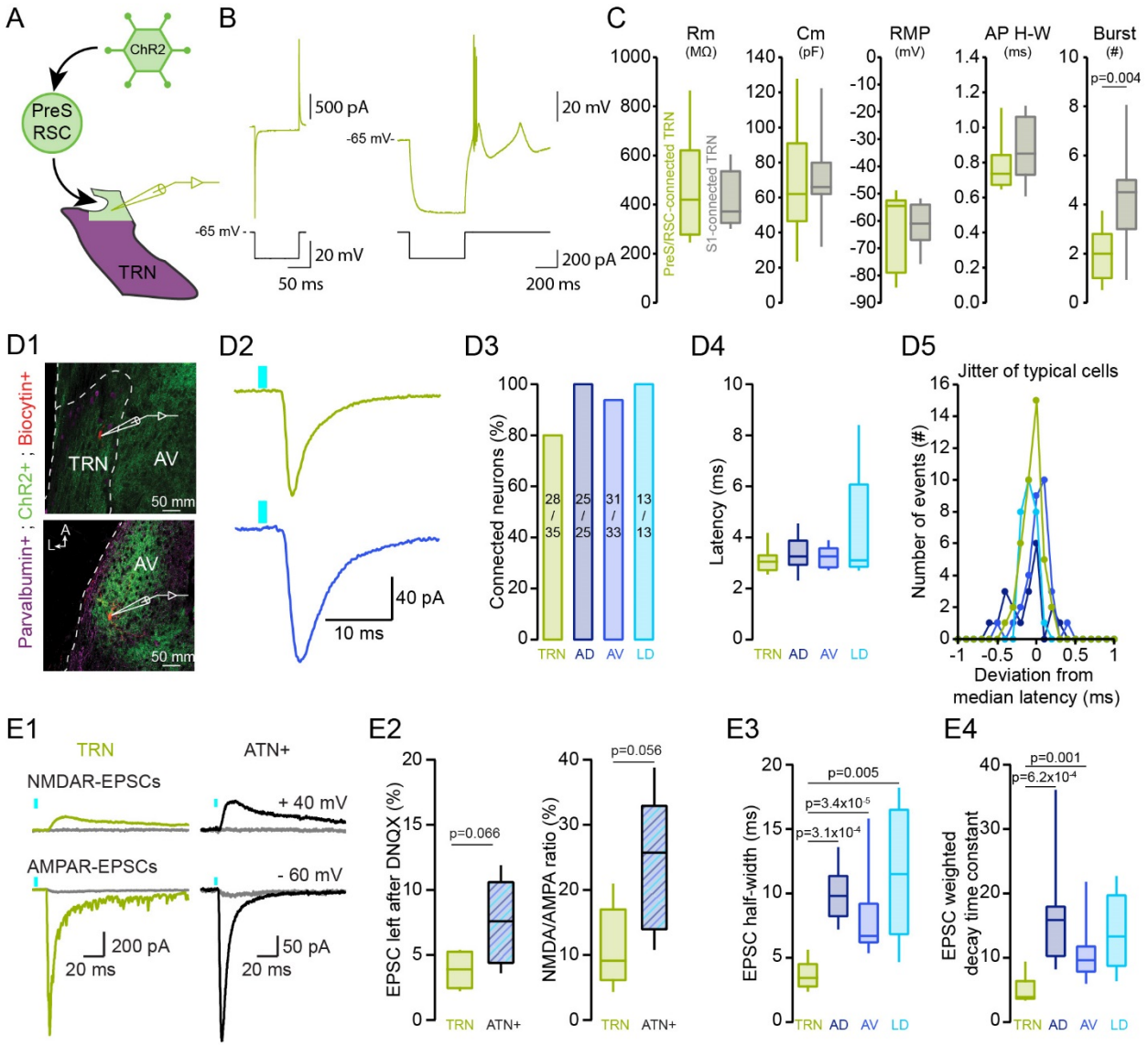

Figure 2. The PreS/RSC establishes functional excitatory synapses onto TRN

(A) Scheme of viral injections (AAV1-CamKIIa-ChR2-EYFP) into PreS/RSC followed by whole-cell patch-clamp recordings. **(B)** Responses of a PreS/RSC-connected TRN neuron (green) to a hyperpolarizing step in voltage-clamp (Left) and to negative current injection in current-clamp (Right). **(C)** Box-and-whisker plots of cellular properties of PreS/RSC-connected (green, n = 16) and, for comparison, S1-connected TRN neurons (grey, n = 11). Data from S1-connected TRN neurons re-used from a previous study (Fernandez et al., 2018). From left to right: membrane resistance (Rm), membrane capacitance (Cm), resting membrane potential (RMP), action potential (AP) half-width (H-W), burst number. Mann-Whitney U tests were used for comparing Rm, RMP and AP H-W, Student's *t* tests for Cm and Burst number. **(D1)** Confocal micrographs of 300 µm-thick mouse brain sections showing the whole-cell recorded TRN (top) and AV (bottom) neurons filled with neurobiotin (red). Green, ChR2-EYFP-expressing PreS/RSC afferents, magenta, PV+ TRN cells. **(D2)** Current responses of TRN (top) and AV (bottom) neurons to optogenetic activation (blue bars, 1 ms, 3.5 mW power, 455 nm) of PreS/RSC afferents, recorded at -60 mV. **(D3)** Connectivity histogram, calculated as the fraction (in %) of neurons responding to optogenetic stimulation. **(D4)** Box-and-whisker plot of response latencies (calculated from LED

onset to response onset) in the TRN (n = 12), AD (n = 16), AV (n = 16) and LD (n = 6). Mann-Whitney U tests and Bonferroni correction: α = 0.0083. **(D5)** Jitter of response latencies (plotted as the deviation from mean for all individual response events) in one cell from TRN, AD, AV and LD across all stimulation trials. **(E1)** Pharmacological analysis of typical evoked excitatory postsynaptic currents (EPSCs) in TRN and ATN+, showing AMPA- and NMDA-EPSCs and their suppression by DNQX (40 μM) and APV (100 μM), respectively (superimposed grey traces). **(E2)** Box-and-whisker plots of DNQX effects (left, in % of original response amplitude, n = 5 for both TRN and ATN+) and of NMDA/AMPA ratios (right). Values of p from Student's *t* tests. **(E3)** Box-and-whisker plot of EPSC half-widths for TRN (n = 7), AD (n = 8), AV (n = 14) and LD (n = 5). Mann-Whitney U tests and Bonferroni correction: α = 0.0083. Statistically significant p values are indicated. **(E4)** Box-and-whisker plot of the EPSC weighted decay time constant in TRN (n = 7), AD (n = 8), AV (n = 14) and LD (n = 5). Same statistical analysis as E3.

PreS/RSC establishes strong unitary connections with driver characteristics onto anterodorsal TRN

TRN and ATN+ neurons were robustly innervated by PreS/RSC afferents, with light-evoked EPSC amplitudes ranging from -25 pA to -1157 pA at high light intensities, although there were nucleus-specific differences (Fig. 3A). Both large and small EPSCs were obtained in slices from the same animals, excluding variable viral transduction as a major reason for this variability. To assess how variability was based on strength and connectivity of PreS/RSC afferents, we used minimal optogenetic stimulation through reducing light intensity to variably evoke failures and successful responses at comparable rates (mean failure rate 47±3 %, at 0.28±0.05 mW) (Fig. 3B1). Unitary PreS/RSC EPSCs of TRN cells were 4- to 5-fold larger than the ones established onto AD and AV cells (Fig. 3B2). Dividing the maximally evoked EPSC amplitude by the unitary one, we calculated ranges of 1 – 9 fibers for TRN, 2 – 32 fibers for AD and 8 – 86 fibers for AV. Therefore, although variable, TRN cells are, on average, targeted by a comparatively small number of fibers, but each with greater unitary strength. A large unitary response size has also been described for cortical projections onto sensory TRN (Cruikshank et al., 2010; Gentet and Ulrich, 2004; Golshani et al., 2001). To determine how many of these fibers were necessary to bring TRN cells to threshold for action potential firing, we performed cell-attached patch-clamp recording to preserve cellular integrity during PreS/RSC synaptic stimulation (Fig. 3C1). Action current numbers showed a steep sigmoidal light dependence with half-maximal values reached at 0.8 mW (Fig. 3C2,C3). Single spikes could be detected at a light intensity corresponding to the one used for minimal stimulation (0.28±0.05 mW). Subsequent whole-cell mode recording in 5 out of 6 cells confirmed that these were bursts of action potentials riding on a low-threshold calcium spike, which showed similar light dependence (half-maximal number of action potentials at 1.1 mW) (Fig. 3C1,C3).

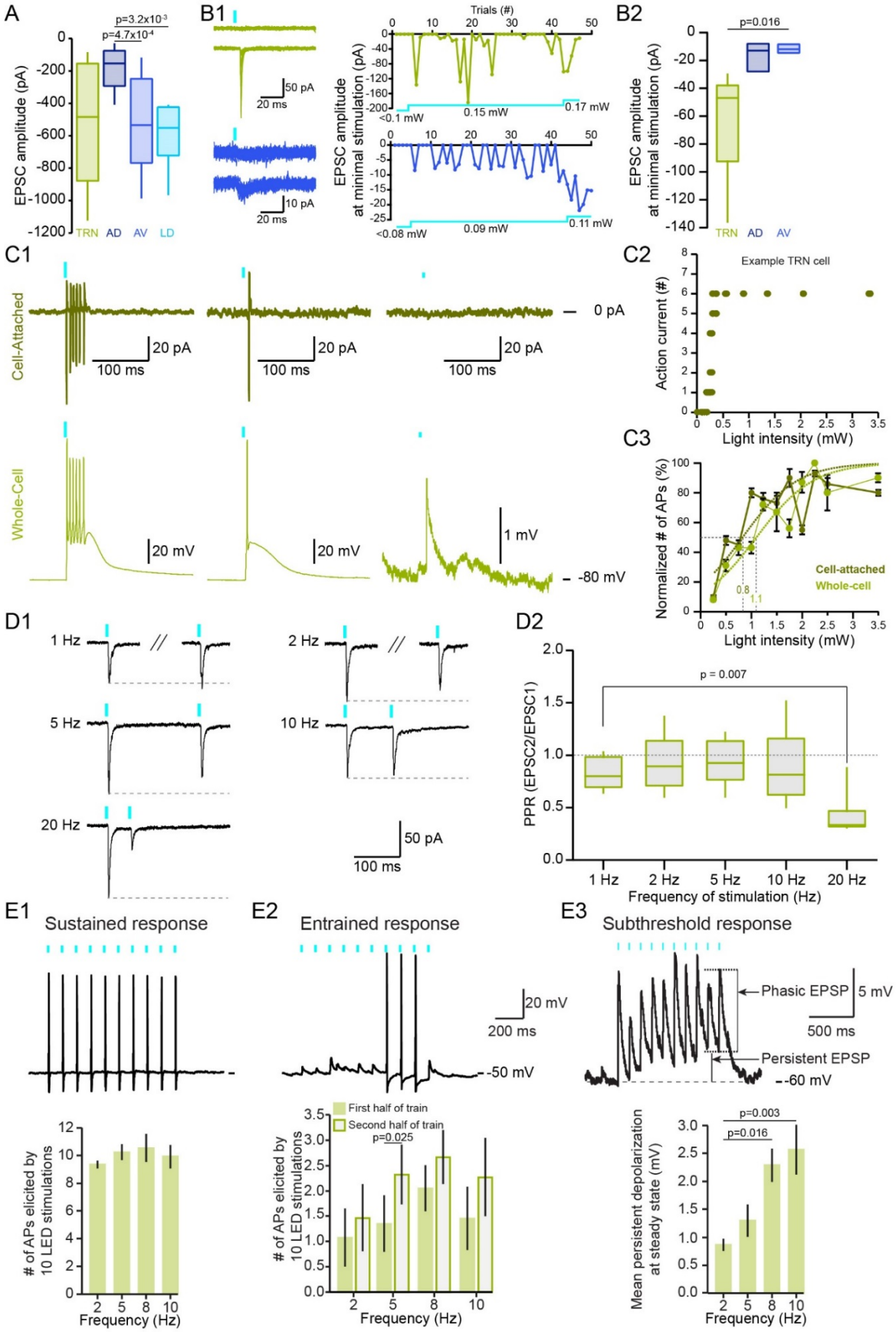
A
p=3.2x10-3
p=4.7x10-4
EPSC amplitude (pA)
TRN AD AV LD
B1
50 pA
20 ms
10 pA
20 ms
Trials (#)
EPSC amplitude at minimal stimulation (pA)
<0.1 mW
0.15 mW
0.17 mW
<0.08 mW
0.09 mW
0.11 mW
B2
p=0.016
EPSC amplitude at minimal stimulation (pA)
TRN AD AV
C1
Cell-Attached
20 pA
100 ms
0 pA
Whole-Cell
20 mV
1 mV
-80 mV
C2
Example TRN cell
Action current (#)
Light intensity (mW)
C3
Normalized # of APs (%)
Cell-attached
Whole-cell
0.8
1.1
Light intensity (mW)
D1
1 Hz
2 Hz
5 Hz
10 Hz
20 Hz
50 pA
100 ms
D2
p = 0.007
PPR (EPSC2/EPSC1)
1 Hz 2 Hz 5 Hz 10 Hz 20 Hz
Frequency of stimulation (Hz)
E1
Sustained response
# of APs elicited by 10 LED stimulations
Frequency (Hz)
E2
Entrained response
20 mV
200 ms
-50 mV
First half of train
Second half of train
p=0.025
# of APs elicited by 10 LED stimulations
Frequency (Hz)
E3
Subthreshold response
Phasic EPSP
5 mV
500 ms
Persistent EPSP
-60 mV
p=0.003
p=0.016
Mean persistent depolarization at steady state (mV)
Frequency (Hz)

216

Figure 3. PreS/RSC establishes strong unitary connections with driver characteristics onto anterodorsal TRN.

(A) Box-and-whisker plot of maximally evoked compound EPSC amplitudes in TRN (n = 12), AD (n = 16), AV (n = 16), LD (n = 6). The intensity of the LED was reduced to ~20 % of the maximum in 4/16 AV and 4/6 LD cells to prevent escape currents. 1-factor ANOVA, $p = 1.25x10^{-3}$, post hoc Student's *t* tests with Bonferroni correction: α=0.0083. **(B1)** Minimal stimulation experiment. Left, overlay of successes and failures for a TRN and an AV neuron in one experiment. Right: Time course of the same experiment. Blue trace: intensity of the light stimulation. At minimal stimulation (0.15 mW for the TRN cell and 0.09 mW for the AV cell), the failure rate was ~50 % (22/39 failures for the TRN neuron, 20/39 failures for the AV neuron). Increasing the light intensity brought the failure rate to 0 % (right part of the graph). **(B2)** Box-and-whisker plot of the amplitude of successfully evoked unitary EPSCs in TRN (n = 5), AD (n = 3) and AV (n = 4). Repeated Mann-Whitney U tests with Bonferroni correction: α = 0.017. **(C1)** Top: representative responses of a cell-attached TRN neuron recording exposed to maximal (left), intermediate (middle) and low (right) light intensities. Bottom: Same experiment in whole-cell current-clamp mode. **(C2)** Graph of action current number for the TRN neuron shown in C1. **(C3)** Same as in C2 for the average of all TRN neurons (cell-attached n = 6, whole-cell n = 5). Data were binned in 0.25 mW light steps. Action current number normalized to the maximum evoked in each neuron. For sigmoidal fits, see Methods. Half-maximal values are indicated. **(D1)** Representative TRN EPSCs at -60 mV upon paired-pulse stimulation at 1, 2, 5, 10 and 20 Hz. Grey dotted lines: amplitude of the first EPSC. **(D2)** Box-and-whisker plot of paired-pulse ratios (TRN: n = 16). Paired Student's t tests or Wilcoxon signed rank-test and Bonferroni correction: α = 0.013. **(E1)** Top: typical membrane voltage response of a TRN neuron to a 10 Hz-light stimulation train. Bottom: Histogram of means (n = 7). Wilcoxon signed rank-tests and Bonferroni correction: α = 0.017. **(E2)** Top: same as in E1 for neurons responding with a subthreshold response at train onset. Bottom: Histogram of means (n = 6). Wilcoxon signed rank-test (at 2 Hz) and Paired Student's *t* tests (at 5, 8, 10 Hz). **(E3)** Top: same as in E1 for subthreshold responses in a TRN neuron held at -60 mV. Bottom: Histogram of the mean persistent depolarization (n = 5). The persistent depolarization measured on the last 3 stimulations. 1-factor RM ANOVA, p = 0.033, post hoc paired Student's *t* tests and Bonferroni correction: α = 0.017.

Single or few active synaptic inputs from PreS/RSC appear thus sufficient to bring TRN cells to threshold through reliable EPSP-low threshold burst coupling.

Excitatory afferents into thalamus have been divided into 2 major groups, drivers and modulators (Sherman, 2017). To start addressing the profile of PreS/RSC afferents, we determined paired-pulse ratios (PPRs) of TRN-and ATN+-EPSCs. Under our ionic conditions, PPRs remained close to 1 until at least 10 Hz (Fig. 3D1,D2, Suppl. Fig. 3). When plotting results from individual experiments, all data points clustered around 1 for 1-10 Hz. This short-term plasticity profile is markedly different from the modulatory profile of cortical input onto sensory TRN, which shows a strong paired-pulse facilitation (PPF) (Fernandez et al., 2018).

At depolarized potentials (-50 mV), where tonic discharge is prevalent, PreS/RSC afferents reliably sustained TRN discharge during stimulation trains (Fig. 3E1). Furthermore, initially

259 subthreshold responses could become suprathreshold in the course of a train (Fig. 3E2), most
260 likely due to temporal summation that gave rise to a persistent depolarization on top of the phasic
261 events (Fig. 3E3). Similar results were found at PreS/RSC-ATN+ synapses (Suppl. Fig. 3).

262

263 **PreS/RSC afferents mediate feedforward inhibition onto ATN+ through recruiting burst**
264 **discharge in PV- and somatostatin (Sst)-expressing TRN cells**

265 How does TRN recruitment by PreS/RSC afferents regulate ATN+ activity? We first tested *in vitro*
266 for Pres/RSC-triggered feedforward inhibition onto ATN+ (Fig. 4A). ATN+ cells were held at
267 voltages to separately monitor EPSC and IPSC components (-60 mV and +15 mV) (see Methods
268 for further details). Out of 22 ATN+ neurons innervated by PreS/RSC, 19 (9 AD, 5 AV, 5 LD)
269 presented with a strong outward current at +15 mV, consistent with an evoked inhibitory
270 postsynaptic current (IPSC) (Fig. 4B). The IPSC latency was higher than the EPSC latency (Fig.
271 4C), consistent with a disynaptic feedforward inhibition. IPSCs were mediated through $GABA_A$
272 receptors (Fig. 4D1,D2). To demonstrate that these IPSCs were indeed mediated by anterodorsal
273 TRN, we combined opto- and chemogenetics in VGAT-Ires-Cre mice expressing the inhibitory
274 Designer Receptor Exclusively Activated by Designer Drugs (inhibitory DREADD, abbreviated as
275 hM4D from here onwards) specifically in the GABAergic cells of anterodorsal TRN and ChR2 in
276 PreS/RSC. Chemogenetic silencing of anterodorsal TRN through bath-application of the hM4D
277 ligand clozapine N-oxide (CNO) while optogenetically activating PreS/RSC afferents indeed
278 reduced the amplitude of the evoked IPSC (Fig. 4E1,E2).

279 The TRN contains subnetworks of PV- or Sst-expressing cells with possibly different functions
280 (Clemente-Perez et al., 2017). We determined the contribution of these subnetworks to ATN+
281 inhibition using PV-Cre and Sst-Cre mice expressing ChR2 in anterodorsal TRN. ChR2-positive
282 fibers were visible throughout the AD, AV and LD in both mouse lines (Fig. 4F), and rapid IPSCs
283 were elicited by activation of both PV- and Sst-expressing TRN cells in all thalamic nuclei (Fig.
284 4G1,G2), suggesting a contribution of both subnetworks to ATN+ inhibition.

285 **Anterodorsal TRN is implied in the tuning of HD cells and contributes to PreS/RSC-induced**
286 **action potential discharge dynamics in ATN+**

287 To study the consequences of PreS/RSC inputs on unit activity of ATN+, we performed *in vivo*
288 single unit recordings in freely behaving mice while optogenetically activating PreS/RSC (Fig. 5A-
289 E). We recorded a total of 77 units in ATN+ (n = 7 mice), out of which 18 were HD units (Fig. 5C),

290 as determined according to standard criteria (Yoder and Taube, 2009) (Suppl. Fig. 4A-C). Firing
291 patterns of single units (n = 61/77 responsive units in ATN+, amongst which 14/18 HD units),
292 analyzed through raster plots, peri-event histograms and z-score analysis of the changes in firing
293 rate compared to baseline (Fig. 5A,B, Methods), fell into 4 distinct classes (Fig. 5D, Suppl. Fig.
294 4). A first major class (n = 26) showed a mixed response composed of an early increase in firing
295 rate that was followed by a decrease and, occasionally, a late increase in firing, reminiscent of a
296 rebound response (Fig. 5A,B). The three other classes showed one of these three response
297 components in isolation (Suppl. Fig. 4). A second small class (n = 3) showed the initial rapid
298 increase in firing rate only. A third large class (n = 18) primarily showed a decrease in firing rate,
299 whereas a fourth class (n = 7) showed only a late increase in firing rate. Time-wise, early increases
300 in firing rate showed an onset latency (relative to the start of the light pulse applied through the
301 optic fibers implanted over PreS/RSC) that was markedly shorter than the decreases and the late
302 increases in firing rate (Fig. 5E). Importantly, HD units responded with similar discharge patterns
303 to PreS/RSC stimulation (Fig. 5D), showing notably decreases in firing rate (8/14 units) and mixed
304 responses (3/14 units). This classification shows that PreS/RSC inputs efficiently control ATN+
305 discharge dynamics with a consistent temporal pattern. Importantly, a substantial fraction of these
306 units responded with transient firing decreases, including also HD units. This pattern is consistent
307 with an inhibitory synaptic input, implying a possible recruitment of anterodorsal TRN, or of other,
308 still unidentified inhibitory feedforward projections.

309 Chemogenetic silencing of anterodorsal TRN was used to directly evaluate the role of TRN
310 inhibition for HD units specifically and for ATN+ firing dynamics more generally.

311 First, we recorded HD units with silicone probes targeted stereotaxically to the AD, the site of HD
312 cells (5 mice, Fig. 5F) (Taube, 1995). We compared the tuning, tuning width, preferred direction
313 and firing rate at the preferred direction of the HD units during a baseline session and 40 min after
314 i.p. injection of CNO (1 – 2 mg/kg) (n = 24) or NaCl (n = 18) (Fig. 5G,H, Suppl. Fig. 5), thereby
315 ensuring that unit properties remained unaltered (see Methods). Overall, we found a decrease in
316 tuning and an increase in the tuning width after CNO injection compared to baseline, whereas
317 preferred direction and maximal firing rate remained unaltered. NaCl injection did not induce
318 changes in any of these four parameters. Therefore, the baseline tuning curve of HD cells in AD
319 in freely moving conditions deteriorates upon a decrease in TRN activity.

320

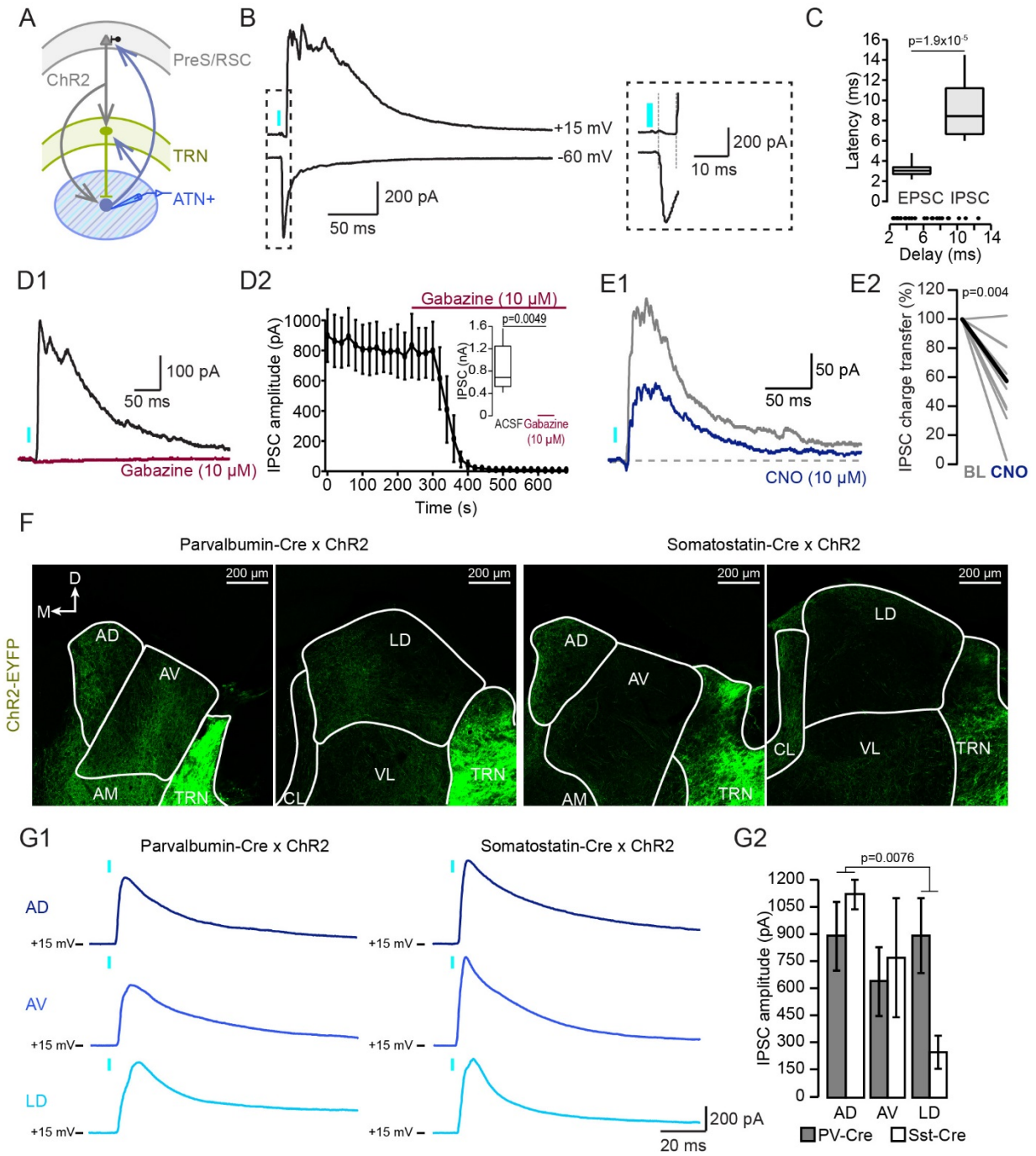

Figure 4. PreS/RSC afferents mediate feedforward inhibition onto anterior thalamus through recruiting burst discharge in PV- and Sst-expressing TRN cells.

(A) Simplified scheme of the hypothesized circuit studied *in vitro*. **(B)** Typical current responses of an ATN+ neuron held successively at -60 and +15 mV to record EPSC and IPSC. Portion indicated by dotted rectangle is expanded on the right. Response latencies (grey vertical lines) were measured from LED onset. **(C)** Top: Box-and-Whisker plot of EPSC and IPSC latencies in ATN+ neurons (n = 24). Bottom: Delays between the onset of the IPSC and the EPSC for all

329 experiments. Wilcoxon signed rank-test. **(D1)** A typical ATN+ IPSC before (black) and after (red)
330 bath-application of the $GABA_A$ receptor antagonist gabazine. **(D2)** Time course of gabazine action
331 (n = 6). Inset: Box-and-Whisker plot of steady-state IPSC amplitude in ACSF and gabazine (paired
332 Student's *t* test). **(E1)** IPSC evoked in an ATN+ neuron of a VGAT-Ires-Cre mouse expressing
333 hM4D in anterodorsal TRN. IPSCs measured before (grey) and after (blue) 10 µM CNO bath-
334 application. **(E2)** Representation of the charge transfer of IPSCs in ATN+ neurons (n = 10).
335 Wilcoxon signed rank-test. **(F)** Confocal micrographs of ChR2-expressing PV-Cre (left) and Sst-
336 Cre (right) coronal brain sections of ATN+. **(G1)** Representative IPSCs elicited in ATN+ neurons
337 held at +15 mV. **(G2)** Histogram of IPSC amplitudes in AD (n = 6 for both PV- and Sst-Cre mice),
338 AV (n = 6 for both) and LD (n = 6 for both). 2-factors ANOVA with factors 'nucleus' and 'cell type',
339 $p = 0.036$ for 'nucleus', $p > 0.05$ for 'cell type', post hoc Student's *t* test with Bonferroni correction:
340 $\alpha = 0.017$ for IPSC amplitude between nuclei regardless of cell type.

341

342 We also chemogenetically silenced anterodorsal TRN while recording from a subset of ATN+
343 units responding to PreS/RSC photostimulation with a decrease in firing rate (n = 15, 8 HD units,
344 7 untuned units) or with an early increase in firing rate (n = 10, 3 HD units, 7 untuned). These
345 units were recorded in three VGAT-Ires-Cre mice expressing hM4D in the TRN and ChR2 in the
346 PreS/RSC. Following a baseline recording session, mice were recorded again 40 min after CNO
347 i.p. injection (Fig. 5I,J, see Methods). After chemogenetic silencing of the TRN, the mean z-score,
348 calculated from onset to offset of significant decrease in firing rate, was significantly reduced (Fig.
349 5K). The latency of decrease in firing rate was not altered in the 11 units in which PreS/RSC
350 stimulation still evoked a significant decrease in firing rate in CNO (Fig. 5L). I.P. injection of CNO
351 did not alter the averaged z-score of the light-evoked early increase in firing rate nor the latency
352 of these events (Fig. 5K,L). These data suggest that the feedforward decrease in firing rate
353 observed in ATN+ units upon PreS/RSC activation is at least partially mediated by the
354 anterodorsal TRN.

355

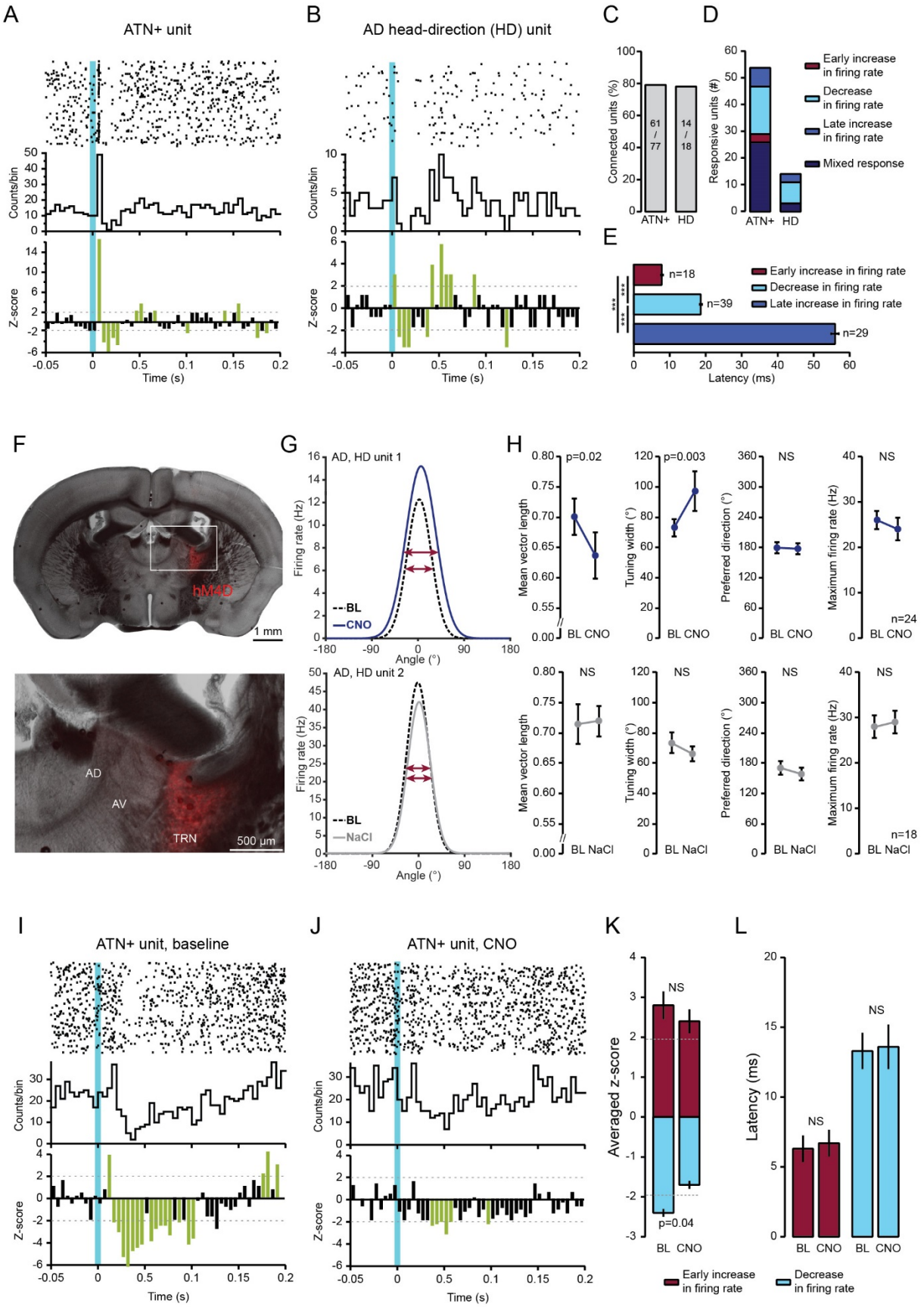
A
ATN+ unit
B
AD head-direction (HD) unit
C
D
Connected units (%)
61 / 77
14 / 18
ATN+ HD
Responsive units (#)
Early increase in firing rate
Decrease in firing rate
Late increase in firing rate
Mixed response
E
n=18
n=39
n=29
Latency (ms)
Counts/bin
Z-score
Time (s)
F
hM4D
1 mm
AD
AV
TRN
500 µm
G
AD, HD unit 1
AD, HD unit 2
Firing rate (Hz)
Angle (°)
BL
CNO
NaCl
H
p=0.02
p=0.003
NS
Mean vector length
Tuning width (°)
Preferred direction (°)
Maximum firing rate (Hz)
BL CNO
BL NaCl
n=24
n=18
I
ATN+ unit, baseline
J
ATN+ unit, CNO
K
Averaged z-score
p=0.04
L
Latency (ms)
Early increase in firing rate
Decrease in firing rate

356

357 **Figure 5. Anterodorsal TRN is implied in the tuning of HD cells and contributes to**
358 **PreS/RSC-induced action potential discharge dynamics in ATN+ .**

359 **(A, B)** Raster plot, cumulative histogram and z-score analysis for two characteristic unit
360 responses. Blue vertical line denotes time of light application. Z-score bins labeled in green
361 highlight significant changes in firing rate. **(C)** Total number of light-responsive ATN+ and HD-
362 tuned units. **(D)** Stacked bar graph showing number of units grouped into four classes based on
363 their response properties. See Suppl. Fig. 4 for further examples. **(E)** Histogram of response
364 latencies. Mann-Whitney U tests and Bonferroni correction: α = 0.017 **(F)** Sections for the
365 anatomical verification of silicone probe implantation in VGAT-Ires-Cre mice expressing the
366 chemogenetic silencer hM4D-mCherry (red) in anterodorsal TRN. **(G)** Examples of HD tuning
367 curves for two units prior to and after injection of CNO or NaCl. Horizontal arrow shows tuning
368 width. **(H)** Quantification of the changes in tuning parameters by CNO or NaCl. Far left: Rayleigh
369 vector length size. Middle left: Width of tuning curve. Middle right: Preferred direction. Right: Firing
370 rate at preferred direction. See Methods for details on analysis and Suppl. Fig. 5 for more
371 examples. Paired Student's *t* tests for Rayleigh vector length size and preferred direction,
372 Wilcoxon signed rank-test for width of tuning curve and firing rate at preferred direction **(I, J)** Same
373 as A, for a unit before (I) and after CNO (J). (**K**) Mean z-scores for early increases (red bar) and
374 decreases (blue bar) in firing rates prior to and after CNO injection. Paired Student's *t* tests. (**L**)
375 Latencies from photostimulation for the same units as in (K), Mann-Whitney U tests.

376 **Anterodorsal TRN inhibition biases navigational search strategies in the Morris water maze**

377 To probe the role of anterodorsal TRN in spatial navigation, we chose the hidden platform version
378 of the Morris water maze (MWM). In this maze, both ATN-dependent and visual cue-dependent
379 allocentric navigational strategies were reported (Garthe and Kempermann, 2013; Stackman et
380 al., 2012). Mice were trained over 10 days to learn the hidden platform in a maze surrounded by
381 visual landmarks, followed by a 10-day reversal learning during which the platform was located in
382 the opposite quadrant (Suppl. Fig. 6A). We hypothesized that chemogenetic suppression of
383 anterodorsal TRN activity, and reduction of PreS/RSC-mediated ATN+ inhibition, would alter
384 navigational behavior once the animal had to rely on HD-dependent strategies. We also asked
385 whether there was a bias in search strategies already in the course of spatial learning.

386 We used two groups of mice: "control" VGAT-Ires-Cre and "hM4D" VGAT-Ires-Cre mice that
387 expressed non-hM4D related proteins or the hM4D specifically in the anterodorsal TRN,
388 respectively (Fig. 6A, Suppl. Fig. 7). In each of the four daily test sessions, entry points into the
389 maze were randomized across the quadrants to enforce the use of allocentric strategies. Both
390 groups became faster swimmers in the course of the task and showed no significant difference in
391 their mean swimming velocity during the 60-s probe sessions (with platform removed), although
392 there was a light trend for control mice to be faster (Fig. 6B). We thus analyzed the proximity to
393 the platform instead of the latency to platform to account for possible effects of differences in swim
394 speed (Awasthi et al., 2019). Based on this measure, both groups performed similarly, as
395 indicated by a comparable decrease of the mean proximity to the platform during test sessions

396

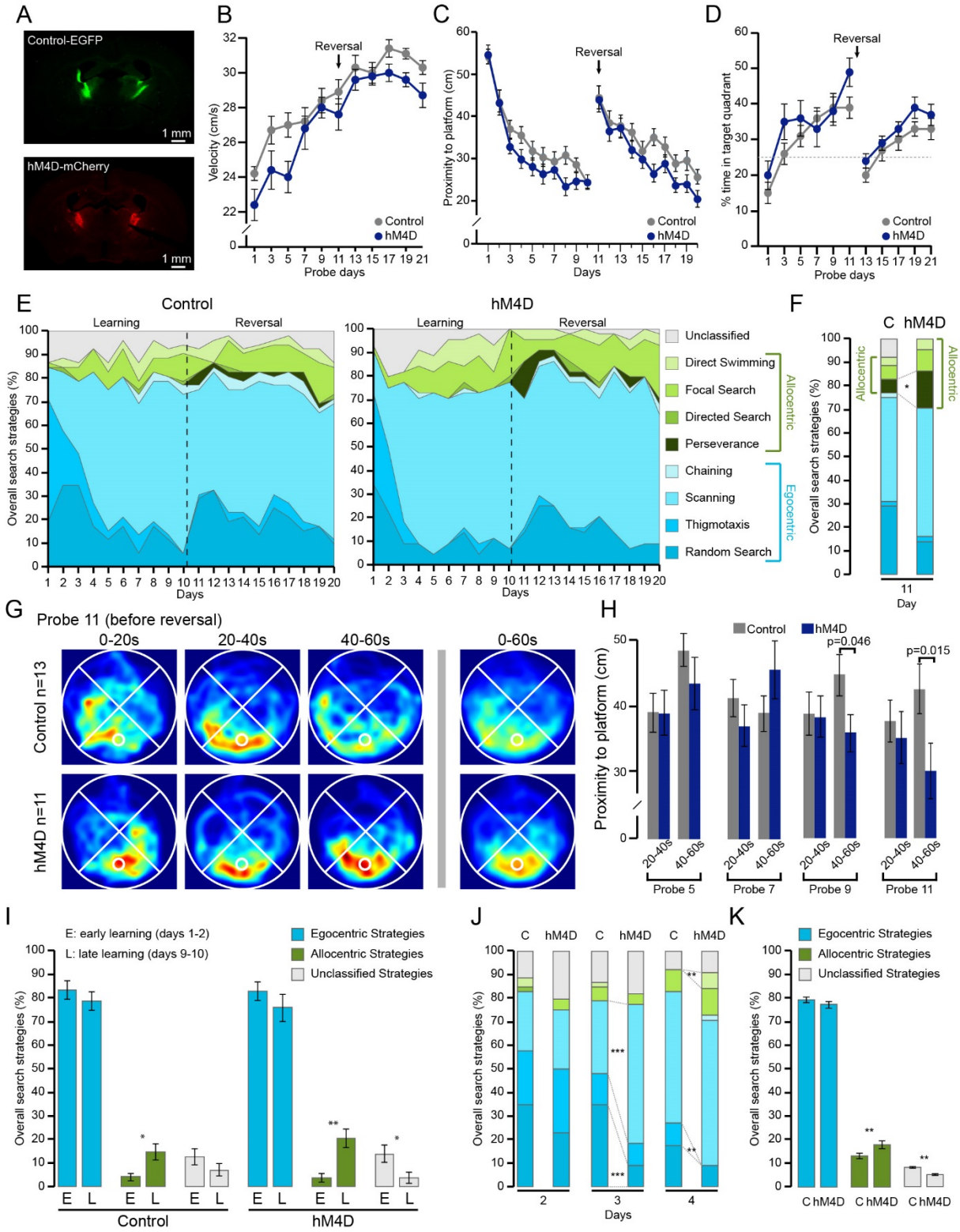
A
Control-EGFP
1 mm
hM4D-mCherry
1 mm
B
Reversal
Velocity (cm/s)
Control
hM4D
Probe days
C
Reversal
Proximity to platform (cm)
Control
hM4D
Days
D
Reversal
% time in target quadrant
Control
hM4D
Probe days
E
Control
hM4D
Learning
Reversal
Overall search strategies (%)
Days
Unclassified
Direct Swimming
Focal Search
Directed Search
Perseverance
Chaining
Scanning
Thigmotaxis
Random Search
Allocentric
Egocentric
F
C hM4D
Allocentric
Overall search strategies (%)
Day
G
Probe 11 (before reversal)
0-20s
20-40s
40-60s
0-60s
Control n=13
hM4D n=11
H
Control
hM4D
p=0.046
p=0.015
Proximity to platform (cm)
20-40s
40-60s
Probe 5
Probe 7
Probe 9
Probe 11
I
E: early learning (days 1-2)
L: late learning (days 9-10)
Egocentric Strategies
Allocentric Strategies
Unclassified Strategies
Overall search strategies (%)
Control
hM4D
J
C
hM4D
Overall search strategies (%)
Days
K
Egocentric Strategies
Allocentric Strategies
Unclassified Strategies
Overall search strategies (%)
C hM4D

397

398

Figure 6. Anterodorsal TRN inhibition biases navigational search strategies in the Morris water maze.

(A) Epifluorescent micrographs of VGAT-Ires-Cre mouse coronal brain sections at Bg -0.8 mm for a control mouse (top) and a test mouse (bottom). Color codes indicate expression products. **(B)** Mean swim velocities of control (n = 13) and hM4D (n = 11) mice during probe sessions. 2-factors RM ANOVA with factor 'day' and 'condition', $p < 2x10^{-16}$ for 'day' and p = 0.04 for 'condition'. Post hoc Student's *t* tests with Bonferroni correction: α = 0.005 for 'condition': not significant. **(C)** Graph of the mean proximity to the platform during training sessions. 2-factors RM ANOVA with factor 'day' and 'condition', $p < 2x10^{-16}$ for 'day' and p = 0.04 for 'condition'. Post hoc Student's *t* tests and Mann-Whitney U tests with Bonferroni correction: α = 0.003 for 'condition': not significant. **(D)** Graph of the percentage of time spent in the target quadrant during probe sessions. Chi-square test against 25% chance, significant at days 1, 7, 9, 11 for Control and days 5, 9, 11, 19, 21 for hM4D. **(E)** Stacked area graphs of search strategies used by control (left) and hM4D (right) mice during trial sessions. **(F)** Proportion of overall strategies at day 11 for control (C) and hM4D (D) mice. Chi-square tests for 'allocentric strategy' and for 'Perseverance', p < 0.05 for both. **(G)** Time-binned (20 s bins) and overall average occupancy plots during the last probe session of the learning phase. Hot colors indicate greater occupancy and are equally calibrated in all plots. **(H)** Histogram of the mean proximity to the platform of control and hM4D mice during binned-probe sessions. Student's *t* test for Control vs hM4D at late time bin (40 – 60 s). **(I)** Averaged proportion of egocentric, allocentric and unclassified strategies used during the early (E, days 1 and 2) and late (L, days 9 and 10) learning phase. Wilcoxon signed rank-tests, p = 0.02 for allocentric strategies in control mice, p = 0.008 and p = 0.03 for allocentric and unclassified strategies in hM4D mice, respectively. **(J)** Proportion of overall strategies at day 2, 3 and 4 for control (C) and hM4D (D) mice. Chi-squared tests for 'Scanning' and for 'Random Search' at day 3, p < 0.001 for both. Chi-square tests for 'Direct Swimming' and for 'Thigmotaxis' at day 4, p < 0.01 for both. **(K)** Averaged proportion of egocentric, allocentric and unclassified strategies used during the whole experiment. Student's *t* test comparing Control (C) vs hM4D (D).

(Fig. 6C). Moreover, from days 5 – 7 of training, the percentage of time spent in the target quadrant was above chance level for both groups during probe sessions (Fig. 6D) These results show an overall comparable, if not slightly better performance of hM4D mice, but they do not provide information about the navigational strategies used. We hence classified swim trajectories on a trial-by-trial basis for all test sessions according to previously described criteria for allo- and egocentric strategies (Suppl. Fig. 6B-D) (Garthe and Kempermann, 2013; Rogers et al., 2017). Figure 6E shows that mice use a mix of trajectories reflecting the use of both ego- and allocentric strategies (Fig. 6E,I,K). Focusing first on early phases of reversal learning (day 11), hM4D mice showed perseverance around the previous platform location, while control animals reverted to trajectories consistent with egocentric strategies (Fig. 6F). If perseverance was indeed reflecting a decreased ability to change navigational strategy once the correct platform location was learned, signs of perseverance should also be seen in the course of learning. Indeed, when inspecting time-binned occupancy plots during probe sessions, hM4D mice persevered searching at the platform position for the whole 60 s-probe session, whereas control mice shifted to a

441 dispersed search pattern of other regions of the pool during the last 20 s of the session. This was
442 particularly the case during the last 2 probe sessions of the learning (beginning of day 9 and 11)
443 (Fig. 6 G,H).

444 Inspired by the finding on the hM4D mice's possibly compromised ability to deploy egocentric
445 strategies during reversal learning, we asked whether evidence for biased strategy selection could
446 also be found during initial platform learning. As is characteristic for the MWM, there was an
447 increase in the proportion of allocentric strategies from day 1-2 to day 9-10 in both control and
448 hM4D mice (Fig. 6 I,J) (Garthe and Kempermann, 2013). However, hM4D mice did so in temporal
449 anticipation, showing significantly more scanning and less random search on day 3, and more
450 direct swimming and less thigmotaxis on day 4 (Fig. 6J). hM4D mice also used an overall greater
451 proportion of allocentric strategies across both learning and reversal learning than control mice
452 (Fig. 6K). Together, suppression of anterodorsal TRN activity 1) alters navigational behavior at
453 reversal learning and 2) biases the search patterns towards allocentric strategies during initial
454 learning.

455

456 ## Discussion

457 Anatomical and physiological identification of synaptic inputs to TRN has repeatedly opened a
458 novel point of view for the TRN's active role in gating sensory information flow to and from the
459 cortex (for review, see (Crabtree, 2018)). We uncover here a previously undescribed excitatory
460 input to TRN from the parahippocampal dPreS and the multisensory-associative RSC. This
461 dPreS/RSC input recruits feedforward TRN inhibition to ATN and to HD-tuned neurons in AD. We
462 thus identify a novel corticothalamic loop that expands the TRN's gating function to the domain of
463 head-orientation signals. Our behavioral experiment indicates that this pathway offers a possible
464 synaptic mechanism contributing to the flexible selection of navigational strategies during spatial
465 navigation. More generally, we favor a view of the TRN as a multi-modal saliency selector that
466 interfaces between acute cognitive demands, such as attentional switching or spatial re-
467 orientation, and the recruitment of the appropriate sensory and HD signals.

468 Retrograde tracing from the anterodorsal portion of the TRN labeled several prefrontal cortical
469 afferents that were described previously (Cornwall et al., 1990; Dong et al., 2019; Lozsádi, 1994).
470 Our novel observation is a continuous band of TRN afferents along the presubicular-retrosplenial
471 axis that starts at the border from subiculum to the PreS, thus at the transition from the three-

472 layered hippocampal to the six-layered parahippocampal complex. These projections arise in
473 deep layers of PreS and RSC, to where projections to ATN were previously retrogradely traced
474 (Wright et al., 2010). Anterodorsal TRN may additionally receive inputs from the centrolateral
475 thalamic nucleus (Krout et al., 2001) and from lateral hypothalamus (Herrera et al., 2016). The
476 functional diversity of these afferents points to the anterodorsal TRN as an assembly of highly
477 integrative neurons that gate thalamic activity appropriately for particular sensory and attentional
478 navigational behaviors.

479 We note here that both RSC and dPreS target LD and AD preferentially, while projections to AV
480 are minor. AD and LD are thought to functionally cooperate within the HD system (Perry and
481 Mitchell, 2019; Simonnet and Fricker, 2018), possibly acting as first- and higher-order nucleus,
482 respectively (Peyrache et al., 2019). The AV, together with the anteromedial nucleus, has been
483 so far associated with a theta-generating system innervated by vPreS (Perry and Mitchell, 2019).
484 The limited spatial resolution of our tracing methods does not currently allow to verify whether
485 anterodorsal TRN is also subdivided into sectors corresponding to this functional subdivision of
486 ATN+. Moreover, the detailed contributions of presubicular, and of the granular and agranular
487 portions of RSC, warrant further investigation. More work is also required to elucidate the detailed
488 organization of the synaptic connectivity from PreS/RSC to anterodorsal TRN and from there to
489 ATN. Interestingly, single-cell labeling identified rat anterodorsal TRN cells with axons bifurcating
490 to innervate both AD and LD (Pinault and Deschênes, 1998). AM-projecting TRN cells were
491 located more ventrally. Anterodorsal TRN may thus contain cells jointly innervating AD and LD,
492 further substantiating a shared function.

493 Our characterization of a cortical excitatory innervation of TRN by PreS/RSC-excitatory input
494 reveals a combination of commonalities but also notable differences to the canonical form of
495 cortical input to sensory TRN that arises from layer 6 corticothalamic neurons of corresponding
496 primary cortex (Usrey and Sherman, 2019). Layer 6 synapses on TRN cells show a high
497 glutamate receptor content (Golshani et al., 2001), high unitary amplitude (Golshani et al., 2001),
498 faster rise and decay times (Gentet and Ulrich, 2004), smaller NMDA/AMPA ratios (Astori and
499 Lüthi, 2013) and marked PPF (Astori and Lüthi, 2013; Castro-Alamancos and Calcagnotto, 1999;
500 Crandall et al., 2015) compared to their thalamocortical counterparts. The presence of PPF is an
501 important criterion to classify layer 6 corticothalamic afferents as modulators rather than drivers
502 (Sherman and Guillery, 1998). While dPreS/RSC-TRN synapses are comparable in terms of
503 unitary amplitude, NMDA/AMPA ratio and EPSC waveform, there is a prominent lack of PPF at
504 dPreS/RSC afferents and a moderate entrainment of firing during repeated stimulation. Rather

505 than being modulators, the PreS/RSC inputs thus share a short-term plasticity profile reminiscent
506 of the driver inputs that count as the principal information-bearing synapses. Top-down driver
507 input is so far known for corticothalamic layer 5 projections to higher-order thalamic nuclei that
508 show a number of morphological hallmarks (Usrey and Sherman, 2019). A driver profile, as we
509 suggest here for the first time for a TRN afferent, implies that anterodorsal TRN conveys direct
510 system-relevant information that is faithfully transmitted to its projection targets. We cannot
511 exclude, however, that PreS and RSC afferents, if stimulated separately, would show different
512 short-term plasticity including PPF and arise from different cortical layers (Simmonet and Fricker
513 2018). A further noteworthy point is that both PV+ and Sst+ TRN neurons innervate the AD, AV
514 and LD with comparable strength, pointing to functional differences compared to sensory first-
515 order thalamic nuclei (Clemente-Perez et al., 2017).

516 When PreS/RSC afferents were activated *in vivo*, a majority of ATN+ units (~79%) and of HD
517 units (77%) responded with changes in action potential firing. We observed sequential firing rate
518 increases and decreases that fall within the time ranges expected for a feedforward inhibition
519 (Crandall et al., 2015). These firing dynamics could result from a mix of afferent mono- and
520 polysynaptic activities because excitatory PreS/RSC neurons project widely to cortical,
521 hippocampal and subcortical targets (Clark et al., 2018; Mitchell et al., 2018; Simonnet and
522 Fricker, 2018), including to the lateral mammillary bodies (Yoder et al., 2015). Potential long-
523 range inhibitory projections that could have been virally transformed also cannot be excluded.
524 However, in strong support of a recruitment of TRN, we show that decreases in firing rate in ATN+
525 and HD units are attenuated once anterodorsal TRN is silenced while all increases in firing rate
526 are preserved. Moreover, the latencies of the initial firing increases and decreases were short and
527 showed little variability from unit to unit, which fits better with a monosynaptic feedforward
528 inhibitory circuit, such as the one recruited by direct TRN activation through PreS/RSC, rather
529 than a polysynaptic one.

530 What could be the functional consequences of PreS/RSC-mediated feedforward inhibition? The
531 precision tuning of the thalamic HD cells is essential for the cortico-hippocampal representation
532 of space (for review, see (Peyrache et al., 2019)). It is distinctly sharper than in the upstream
533 lateral mammillary body (Blair et al., 1998), suggesting that active inhibition is at work at thalamic
534 levels to suppress firing at angles outside the preferred direction. TRN is a likely candidate for
535 this inhibition, because, as we show, the HD tuning of AD cells degrades with a silenced TRN. As
536 the effect size we measure is comparable to the one observed after PreS lesion (Goodridge and
537 Taube, 1997), PreS-dependent TRN regulation could act in a circuit analogous to that of

538 descending corticothalamic control of thalamic sensory receptive fields (Temereanca and
539 Simons, 2004). Sharpening could also arise via recurrent synaptic activity between TRN and AD
540 to coordinate activity in similarly tuned HD neurons (Peyrache et al., 2015). Once important visual
541 landmark information has to processed by the HD system, PreS/RSC could act through TRN to
542 enforce AD discharge in response to novel cues, thereby helping to reset the tuning via generating
543 inhibition-rebound firing. Consistent with this disynaptic circuit, it has been shown that updating
544 of HD tuning occurs rapidly (< 100 ms), which requires short synaptic delays (Zugaro et al., 2003).
545 Moreover, there is now first evidence that acute optogenetic inhibition of TRN indeed prevents
546 the updating of HD units to rapidly changing environments (Duszkiewicz et al., 2019). TRN-driven
547 ATN bursting might also be an important component in oscillatory patterns observed within ATN+,
548 such as the one proposed to occur in AD (Peyrache et al., 2019; Peyrache et al., 2015) or in AV
549 (Tsanov et al., 2011), which are probably relevant for linking spatial information to hippocampal
550 memory processing.

551 To date, behavioral evidence for a role of the HD system in behavioral navigation is limited (Butler
552 et al., 2017; Taube et al., 1992; Valerio and Taube, 2012; van der Meer et al., 2010) and the role
553 of specific HD circuits, including dPreS and RSC, just starts to be behaviorally explored.
554 Experimental effort typically targets egocentric strategies, for example by moving the MWM
555 relative to landmarks between trials (Stackman et al., 2012), by studying navigation in darkness
556 (Yoder et al., 2019) or by putting rats upside down (Calton and Taube, 2005). In contrast, the idea
557 that spatial navigation requires an on-going switching between a range of possible strategies has
558 not been much pursued, although it is known for human studies (Miniaci and De Leonibus, 2018).
559 For example, a recent study using a hippocampus-specific synaptic knockout animal interpreted
560 perseverant behavior at the platform location as a lack of forgetting (Awasthi et al., 2019), but the
561 question of possible bias in navigational strategies was not addressed. Trajectory analysis in the
562 MWM thus offers itself as an interesting approach to follow on the evolution of navigational
563 behavior under well-controlled landmark conditions while simultaneously allowing egocentric
564 strategies (Dolleman-van der Weel et al., 2009; Garthe and Kempermann, 2013). We found a
565 preferential use of allocentric strategies when anterodorsal TRN was suppressed, suggesting that
566 egocentric navigation was less efficient. This is reminiscent of an ATN lesion study (Stackman et
567 al., 2012) and goes along with preserved visual and motor behaviors of the swimming animals.
568 Therefore, it is also unlikely that TRN-dependent inhibitory effects on nuclei other than ATN, such
569 as on intralaminar nuclei to attenuate escape responses, (Dong et al., 2019), are primary causes
570 for the change in search strategies. Anterodorsal TRN activity seems to be critically required at
571 moments when there is a mismatch between allocentric cues and new platform location, such

572 that novel relations between external landmarks and navigational strategies, which depend on
573 HD cells, have to be built. Interestingly, the RSC has been proposed as an area involved in
574 allocentric navigation and memory formation, but also in the switching between allo- and
575 egocentric strategies to optimize navigational goals (Mitchell et al., 2018). In particular, its strong
576 connections to limbic thalamus have been implied in the solving of spatial problems (Clark et al.,
577 2018). Similar more complex roles in spatial navigation have recently been proposed for dPreS
578 (Yoder et al., 2019), which has been primarily analyzed as part of the hierarchy of the egocentric
579 coding system (Dumont and Taube, 2015; Peyrache et al., 2017; Taube et al., 1990). Our work
580 does not currently disentangle between the distinct roles of these two brain areas. However, it
581 has managed to pinpoint to the existence of a possibly fine switching mechanism at the interface
582 between major brain areas that, when perturbed, preserved overt navigational performance but
583 compromised it at challenging moments that could pose existential threats.

584 This work integrates TRN function into the brain's control of sensory-guided spatial navigation.
585 The anterodorsal sector of TRN, located at the *limbus*, the 'edge' of the TRN, is a site of complex
586 integration where navigational, attentional, motor and emotional information may be combined for
587 precise control of anterior thalamus-dependent navigational systems. As a perspective arising
588 from this work, we suggest that neuropsychological screening for deficits in navigational flexibility
589 may be useful in the diagnosis of disorders linked to TRN dysfunction, such as in
590 neurodevelopmental disorders linked to attentional deficits (Krol et al., 2018) and in schizophrenia
591 (Wilkins et al., 2017).

592 Acknowledgements

593 We thank Andreas Lüthi for providing training for the multiwire recordings, Adrien Peyrache for
594 providing training for the silicone probes, Cyril Herry for helping with single unit sorting and
595 analysis, Leonardo Restivo for helping with the design of the Morris water maze experiment and
596 careful reading of the manuscript, Christian Lüscher for providing the VGAT-Ires-Cre mouse line,
597 Desdemona Fricker, John Huguenard, Ralf Schneggenburger for constructive discussions,
598 Simone Astori for critical reading of the manuscript, all lab members for constructive input for the
599 manuscript and discussions in the course of the project.

600 Funding: GV received Travel Grants from the Jean Falk Vairant Foundation, Life Sciences
601 Switzerland and Swiss Society for Neuroscience, ZR was supported by the Marie Heim Vögtlin
602 Foundation, AG received an Erasmus Mobility Grant, AL was supported by Swiss National
603 Science Foundation (Grant No. 31003A-166318 and 310030-184759) and Etat de Vaud.

604 ## Author contributions

605 GV carried out and analyzed all experimental tracing, *in vitro*, *in vivo* and behavioral data, and
606 also contributed to the design of the *in vivo* and behavioral experiments. ZR gained first evidence
607 for the anatomical connectivity between dPreS/RSC and anterodorsal TRN and initiated the *in*
608 *vivo* unit recordings. RC wrote the Matlab code for the analysis of head-direction data and MWM
609 Strategy. EB contributed to viral injections and the MWM experiments, GK to the antero- and
610 retrograde tracing data. AG carried out the *in vitro* recordings in PV- and Sst-Cre mice. VP
611 assisted with anatomical analysis. LMJF contributed to the surgery and analysis for *in vivo*
612 experiments. AL supervised the project and wrote the manuscript with contribution of GV.

613 ## Declaration of interests

614 The authors declare no competing interests.

615 ## STAR Methods

616 **Animal husbandry and ethical approval**

617 We used mice of either sex from the C57BL6/J line and from the Slc32a1$^{tm2(cre)Lowl}$ line, commonly
618 referred to as VGAT-Ires-Cre line (Jackson Labs, generated by Dr. B. Lowell, Beth Israel
619 Deaconess Medical Center, Harvard) (Vong et al., 2011), male
620 C57Bl/6J;129P2_Pvalbtm1(cre)Arbr/J mice, referred to here as PV-Cre mice, and male B6N.Cg-
621 Sst<tm2.1(cre)Zjh>/J mice, referred to here as Sst-Cre mice. These three transgenic lines
622 express the Cre-recombinase either in VGAT-, PV- or Sst-positive neurons, respectively. All
623 animals were housed in a temperature and humidity-controlled animal house with a 12/12 h light-
624 dark cycle (lights on at 9 a.m.) and water and food available *ad libitum.* The VGAT-Ires-Cre line
625 was originally generated on a mixed C57BL/6;FVB;129S6 genetic background and backcrossed
626 to C57BL6 ever since. PV-Cre and Sst-Cre lines were maintained on a C57BL6 background.
627 VGAT-Ires-Cre and PV-Cre were used as homozygous, whereas the Sst-Cre mice were
628 heterozygous. For anatomical tracing (retrograde and anterograde), mice (n = 24) were
629 transferred into a housing room with similar conditions on the day prior to injection. They remained
630 there for 7 days after injection before perfusion and tissue processing. For viral injections, mice
631 were transferred into a P2 safety level housing with similar conditions on the day prior to the
632 injection. They remained there 3 – 5 weeks before being used for *in vitro* electrophysiology (n =
633 57), 2 – 3 weeks before surgical implantation for *in vivo* electrophysiology (n = 9), and 2 – 3 weeks
634 before behavioral experiments (n = 24, only males). All experimental procedures complied with

635 the Swiss National Institutional Guidelines on Animal Experimentation and were approved by the
636 Swiss Cantonal Veterinary Office Committee for Animal Experimentation.

637

638 **Anatomical tracing and verification of recording and injection sites**

639 Retrograde tracing

640 C57BL6/J mice, 4- 8-week-old, were anesthetized with 5 % isoflurane and fixed onto the
641 stereotaxic frame. During the surgery, the anesthesia level was reduced to 1- 3 % and N_2O was
642 added if the surgery lasted > 1 h. Analgesia was ensured through Carprofen (5 mg/kg i.p.).
643 Craniotomies were performed above the sites of injection at (anteroposterior (AP), mediolateral
644 (ML), depth from cortical surface (DV), in stereotaxic coordinates from Bregma): -0.7, ±1.5, -3.1
645 to target the anterodorsal TRN. Glass pipettes (5-000-1001-X, Drummond Scientific, Broomall,
646 PA) were pulled on a vertical puller (Narishige PP-830, Tokyo, Japan) and backfilled by capillarity
647 with fluorescent latex microspheres (Red Retrobead™, Lumafluor). Using a Picospritzer III,
648 pressurized air pulses (15 psi, 10 ms) were applied every 10 s for 10 min to inject the retrobeads.
649 After 4 – 7 days, mice were perfused and their brains collected for immunostainings.

650 Anterograde tracing

651 The anesthetic and surgical procedures were the same as the ones used for retrograde tracing.
652 The coordinates of injection were (AP, ML, DV): -3.8, ±1.6, -1.0 for RSC, -3.8, ±2.3, -1.6 for PreS.
653 Glass pipettes were backfilled by capillarity with the plant lectin anterograde tracer *Phaseolus*
654 *vulgaris*-leucoagglutinin (PHAL-L, Vector Laboratories, Cat. No. L-1110). PHAL-L was chosen as
655 it permits focal labeling with little spread, which seemed appropriate to target PreS and RSC as
656 specifically as possible. A chlorinated silver wire was inserted into the pipette and a reference
657 electrode attached to the mouse tail. The PHAL-L was electroporated with a 5-µA current, 7 s
658 on/off loop for 20 min, applied with a home-made current isolator and a Master-8 (Master-8 Pulse
659 Stimulator, A.M.P.I., Jerusalem, Israel). After 5 – 7 days, mice were perfused and their brains
660 collected for immunostainings.

661 Perfusion and tissue processing

662 Mice were injected i.p. with a lethal dose of pentobarbital. Intracardial injection of ~45 ml of
663 paraformaldehyde (PFA) 4 % was done at a rate of ~2.5 ml/min. Brains were post-fixed in PFA 4
664 % for at least 24 h at 4°C. Brains were sliced with a Vibratome® (Microtome Leica VT1000 S,

665 section thickness: 100 µm, speed: 0.25-0.5 mm/s and knife sectioning frequency: 65 Hz) in 0.1 M
666 phosphate buffer (PB). Brain sections were either directly mounted on slides or disposed in
667 twelve-well plates filled with 0.1 M PB for immunohistochemistry.

668 Immunofluorescent labeling

669 100 µm-thick brain sections were washed 3 times in 0.1 M PB and transferred to a blocking
670 solution containing 0.1 M PB, 0.3 % Triton, 2 % normal goat serum (NGS) for 30 min. The first
671 antibody solutions also contained 0.1 M PB, 0.3 % Triton, 2 % NGS. For PHAL-L injected mice,
672 we added 1:8000x of rabbit anti-PHAL-L (Vector Laboratories, AS-2300, RRID: AB_2313686) and
673 1:4000x of mouse anti-PV (Swant, PV235, RRID: AB_10000343). For retrobead-injected and
674 virally injected PV-Cre and Sst-Cre mice, we added 1:4000x of mouse anti-PV (Swant, PV235,
675 RRID: AB_10000343). Sections were kept at 4°C for 48 h on a shaking platform. After 3 washings
676 in 0.1 M PB, we added a secondary antibody solution containing 0.1 M PB, 0.3 % Triton, 2 %
677 NGS and, when appropriate, 1:500x of goat anti-rabbit Cyanine Cy3™ (Jackson Immunoresearch,
678 111-165-003, RRID: AB_2338000), 1:500x of goat anti-mouse Cy5™ Jackson Immunoresearch,
679 115-175-146, RRID: AB_2338713) and/or 1:500x of goat anti-mouse Alexa Fluor® 488 (Jackson
680 Immunoresearch, 115-545-003, RRID: AB_2338840). Sections were mounted on slides and
681 covered with a mounting medium (Vectashield).

682 300 µm-thick brain sections obtained from patch-clamp recording sessions were post-fixed in 4
683 % PFA for at least 24 h. Brain sections were washed 3x in 0.1 M PB and then pretreated with a
684 solution containing 0.1 M PB and 1 % Triton for 30 min. The blocking solution was 0.1 M PB, 1 %
685 Triton, 2 % NGS and was applied for 30 min. The first antibody solution contained 0.1 M PB, 1 %
686 Triton, 2 % NGS, 1:4000x mouse anti-PV (Swant, PV235, RRID: AB_10000343) and was applied
687 for 5 days at 4°C. The secondary antibody solution contained 0.1 M PB, 0.3 % Triton, 2 % NGS,
688 1:500x goat anti-mouse CY5, (Jackson ImmunoResearch, 115-175-146, RRID: AB_2338713),
689 1:8000x Streptavidin ALEXA594 (Jackson ImmunoResearch, 016-580-084, RRID: AB_2337250)
690 and was applied for 24 h at 4°C. Sections were mounted on slides and covered with a mounting
691 medium (Vectashield).

692 Microscopy

693 Electromicrographs of brain slices were taken with a fluorescent stereomicroscope (Nikon SMZ
694 25) or a confocal microscope (Zeiss LSM 780 Quasar Confocal Microscope). NIS-Elements 4.5
695 (Nikon), Adobe Photoshop CS5 and Zen lite 2012 were used to merge images from different
696 channels.

697

698 **Viral injections**

699 Mice 3- 5-week-old were anesthetized using Ketamine-Xylazine (83 and 3.5 mg/kg, respectively)
700 and placed on a heating blanket to maintain the body temperature at 37°C. An initial dose of
701 analgesic was administrated i.p. at the beginning of the surgery (Carprofen 5 mg/kg). The animal
702 was head-fixed on a stereotactic apparatus equipped with an ear and mouth adaptor for young
703 animals (Stoelting 51925, Wood Dale, IL). The bone was exposed at the desired injection site
704 through a small skin incision. Viruses were injected with a thin glass pipette (5-000-1001-X,
705 Drummond Scientific, Broomall, PA) pulled on a vertical puller (Narishige PP-830, Tokyo, Japan).
706 C57BL6/J mice were injected bilaterally with a virus encoding ChR2 (500 nl of AAV1-CaMKIIa-
707 ChR2(H134R)_eYFP-WPRE-hGH, 10^{12} GC, ~100–200 nl/min) into the PreS (AP, ML, DV): -3.8,
708 +/-2.5, -1.7. VGAT-Ires-Cre mice were injected uni/bilaterally with 500 nl of AAV1-CamKIIa-
709 ChR2(H134R)_eYFP-WPRE-hGH ($1x10^{12}$ GC, ~100–200 nl/min) into the PreS and/or
710 uni/bilaterally with a virus encoding hM4D -mCherry (500 nl of AAV8-hSyn-DIO-
711 hM4D(Gi)_mCherry, $6.4x10^{12}$ GC), or hM4D -IRES-mCitrine (500 nl of ssAAV8/2-hSyn1-dlox-
712 A_hM4D(Gi)_IRES_mCitrine-dlox-WPRE-hGHp(A), $3.1x10^{12}$ GC) or a control AAV8 encoding a
713 hM4D -unrelated construct (500 nl of AAV8-hSyn-FLEX-Jaws_KGC_GFP_ER2, $3.2x10^{12}$ GC) in
714 the anterior sector of the TRN (AP, ML, DV: -0.8, ±1.35, -3.1). PV-Cre and Sst-Cre mice were
715 injected into the anterior TRN (AP, ML, DV: -0.8, ±1.35, -3.1) with AAV1-EF1a-DIO-
716 ChR2(H134R)_eYFP-WPRE-hGH ($1x10^{12}$ GC, 500 nl, ~100–200 nl/min).

717

718 ***In vitro* electrophysiological recordings**

719 Slice preparation, solutions and recordings.

720 Brain slice preparation, storage and recordings were performed essentially as described
721 (Fernandez et al., 2018). Adult 8- 10-week-old C57BL6/J and VGAT-Ires-Cre mice (3 – 4 weeks
722 post viral injection) were briefly anesthetized with isoflurane and their brains quickly extracted.
723 Acute 300-µm-thick coronal brain slices were prepared in ice-cold oxygenated sucrose solution
724 (which contained in mM: 66 NaCl, 2.5 KCl, 1.25 NaH_2PO_4, 26 $NaHCO_3$, 105 D(+)-saccharose, 27
725 D(+)-glucose, 1.7 L(+)-ascorbic acid, 0.5 $CaCl_2$ and 7 $MgCl_2$), using a sliding vibratome (Histocom,
726 Zug, Switzerland). Slices were kept for 30 min in a recovery solution at 35°C (in mM: 131 NaCl,
727 2.5 KCl, 1.25 NaH_2PO_4, 26 $NaHCO_3$, 20 D(+)-glucose, 1.7 L(+)-ascorbic acid, 2 $CaCl_2$, 1.2 $MgCl_2$,

728 3 myo-inositol, 2 pyruvate) before being transferred to room temperature for at least 30 min before
729 starting the recording. Slices were placed in the recording chamber of an upright microscope
730 (Olympus BX50WI, Volketswil, Switzerland) and continuously perfused at room temperature with
731 oxygenated ACSF containing (in mM): 131 NaCl, 2.5 KCl, 1.25 NaH_2PO_4, 26 $NaHCO_3$, 20 D(+)-
732 glucose, 1.7 L(+)-ascorbic acid, 2 $CaCl_2$ and 1.2 $MgCl_2$. This solution was supplemented in all
733 experiments with 0.1 picrotoxin, 0.01 glycine, with picrotoxin removed for the recordings testing
734 for feedforward inhibition (see Fig. 4). Borders of anterior TRN and ATN+ were visually identified
735 in transillumination using a 10x water-immersion objective. Within a selected nucleus, cells were
736 visualized through differential interference contrast optics a 40x water-immersion objective.
737 Infrared images were acquired with an iXon Camera X2481 (Andor, Belfast, Northern Ireland).
738 Cells were patched using borosilicate glass pipettes (TW150F-4) (World Precision Instruments,
739 Sarasota, FL) pulled with a DMZ horizontal puller (Zeitz Instruments, Martinsried, Germany) to a
740 final resistance of 2.5-5 MΩ. A K^+-based intracellular solution that contained (in mM) 140
741 KGluconate, 10 Hepes, 10 KCl, 0.1 EGTA, 10 phosphocreatine, 4 Mg-ATP, 0.4 Na-GTP, pH 7.3,
742 290–305 mOsm, supplemented with ~2 mg/ml of neurobiotin (Vector Labs, Servion, Switzerland)
743 was used for comparative measurements of the passive cellular properties (Fig. 2B,2C), for the
744 cell-attached recordings (Fig. 3C) and for all current-clamp recordings (Fig. 3E). A Cs^+-based
745 intracellular solution containing (in mM) 127 CsGluconate, 10 Hepes, 2 CsBAPTA, 6 $MgCl_2$, 10
746 phosphocreatine, 2 Mg-ATP, 0.4 Na-GTP, 2 QX314-Cl, supplemented with ~2 mg/ml of
747 neurobiotin, pH 7.3, 290–305 mOsm) was used with all the other voltage-clamp protocols. For
748 these solutions, a liquid junction potential of -10 mV was taken into account for the current-clamp
749 data. Signals were amplified using a Multiclamp 700B amplifier, digitized via a Digidata1322A and
750 sampled at 10 kHz with Clampex10.2 (Molecular Devices, San José, CA).

751 Recording protocols, optogenetic stimulation and analysis.

752 Immediately after gaining whole-cell access, cell resistance (R_m) and cell capacitance (C_m) were
753 measured in voltage-clamp at -60 mV through applying 500 ms-long, 10-20 mV hyperpolarizing
754 steps (5 steps/cell). Then the recording was switched to current-clamp to measure the resting
755 membrane potential (RMP). Squared somatic current injections (-50 to -300 pA for 500 ms, 4
756 injections/cell) hyperpolarized neurons below -100 mV from membrane potentials between -50 to
757 -60 mV and induced repetitive burst discharge in TRN neurons and single burst discharge in
758 thalamic neurons (Fig. 2B, 2C). Squared current injections of increasing amplitude (step size, 50
759 pA, 500 ms) were used to depolarize the neurons and generate tonic firing. Action potential
760 properties were measured at the rheobase.

761 Whole-field blue LED (Cairn Res, Faversham, UK) stimulation (455 nm, duration: 0.1 to 1 ms,
762 maximal light intensity 3.5 mW, 0.16 mW/mm^2) in voltage-clamp (-60 mV) was used to assess the
763 connectivity of TRN and ATN+ neurons through fibers arising from the PreS/RSC. EPSCs were
764 elicited through single light pulses every 20 s, with a 5 mV hyperpolarizing step to control for the
765 access resistance. After a stable baseline of > 2 min, drugs were applied in the bath (40 µM
766 DNQX, 100 µM D,L-APV). To measure NMDA-components, the holding membrane potential was
767 slowly brought to +40 mV where NMDAR-mediated currents were recorded for 2 min before bath-
768 application of D,L-APV. Single light pulses were used in protocols to measure EPSC kinetics and
769 pharmacological properties (Fig. 2D, 2E). The latency from LED onset, EPSC half-width and
770 EPSC weighted decay time constant were measured with Clampfit 10.2. The effect of bath-
771 application of 40 µM DNQX was measured once the reduction of EPSC amplitude reached a
772 steady state. The NMDA/AMPA ratio was measured by dividing the amplitude of the EPSC at +40
773 mV in DNQX by the amplitude of the EPSC at -60 mV during the baseline and was expressed in
774 percentage.

775 Minimal stimulation was achieved by progressively reducing the intensity of a single light pulse
776 from its maximum (3.5 mW) to a level where only ~50 % of the stimuli induced a successful EPSC.
777 The light intensity potentiometer allowing a limited graduation of light intensities, we could include
778 only a few cells (n = 12/50) in which this condition was achieved at 0.28±0.05 mW. In the case of
779 LD neurons, which showed very high amplitude EPSCs with frequent escape currents, none of
780 them reached the criterion to be included. Minimal stimulation was observed for light intensities
781 averaging 0.28±0.05 mW, less than 10 % of the maximum. In a subset of cells (n = 8), we slightly
782 increased light intensity to 0.40±0.08 mW to verify whether failure rate decreased but the
783 amplitude of successful responses was maintained. This was achieved in 5 cells in which failure
784 rate decreased to 0 % but the amplitude of successes was 109±4 % of that found during minimal
785 stimulation, whereas it increased to > 140 % in the remaining 3 cases. All successful EPSCs at
786 minimal light stimulation were visually identified and measured in Clampfit10.2.

787 Cell-attached recordings of TRN cells (Fig. 3C) were achieved with recording pipettes of ~5 MΩ
788 resistance, voltage-clamped at 0 mV and ~0 pA of holding current, while applying single light
789 stimuli at varying light intensity (~100 stimuli/cell, one every 10 s). Whole-cell access was then
790 established and cells held in current-clamp at their resting membrane potential. Single light
791 stimulations with similar light intensities were given ~30 times for each cell every 10 s. The number
792 of action currents/action potentials and the interspike interval (ISI) were manually measured on
793 Clampfit10.2. The number of spikes was normalized to the maximum number evoked by the light

794 stimulation. Data were grouped in bins of 0.25 mW of light (Fig. 3C3) and a sigmoidal fit was
795 applied using Igor Pro 7 (WaveMetrics Inc., Lake Oswego, OR). The sigmoidal fit for cell-attached
796 evoked spikes was $= \frac{100}{1+e^{\frac{-(x-0.82)}{0.54}}}$. The sigmoid fit for whole-cell evoked spikes was $= \frac{100}{1+e^{\frac{-(x-1.1)}{0.56}}}$.

797 Paired light stimulations at 1, 2, 5, 10 and 20 Hz were used to assess the short-term plasticity of
798 PreS/RSC-TRN and PreS/RSC-ATN+ synapses. The paired pulse ration (PPR) was expressed
799 as the ratio between the second and the first EPSC amplitude (Fig. 3D). Four responses were
800 elicited for each frequency, with an interval of 20 s between each protocol. The amplitude of
801 EPSCs was measured on the average trace in Clampfit10.2, and traces were not included if
802 spontaneous currents appeared in between the paired stimuli.

803 For train stimulation, PreS-RSC afferents to TRN and ATN+ neurons were stimulated with 10 light
804 pulses delivered 1/30 s at 2, 5, 8 and 10 Hz while cells were held at -50 to -60 mV in current-
805 clamp (Fig. 3E). Per stimulation frequency and cell, 5 responses were recorded and averaged.
806 Responses were subdivided into sustained (Fig. 3E1) or entrained (Fig. 3E2) responses based
807 on whether or not the first light pulse elicited an action potential. The number of action potentials
808 generated by the train of stimulation was counted on Clampfit10.2. To quantify sustained and
809 entrained responses, the number of action potentials during the 5 first stimulations was compared
810 to the number of action potentials during the 5 last stimulations. In subthreshold responses, the
811 amplitudes of the phasic responses were calculated from the point of positive inflection after a
812 light stimulation to the next positive peak for each of the 10 subthreshold responses. The
813 persistent depolarization was measured as the difference between the baseline value before the
814 train of stimulation and the point of positive inflexion after each light stimulation. The mean
815 persistent depolarization for the last 3 stimulations was used to quantify the steady state
816 response.

817 To record feedforward inhibitory currents, using the Cs-based intracellular solution defined above,
818 we studied single light-evoked EPSCs recorded in ATN+ cells at -60 mV (uncorrected for a 10
819 mV junction potential). Then the membrane potential of the cell was slowly brought to +15 mV
820 (uncorrected for a 10 mV junction potential). In 6 ATN+ cells, IPSCs were recorded for 4 min (12
821 protocols, once every 20 s) for a baseline, then 10 µM gabazine were bath-applied. The amplitude
822 of the IPSCs in gabazine was measured at the steady state. A similar protocol was applied for 10
823 ATN+ cells recorded in VGAT-Ires-Cre mice expressing the hM4D in TRN cells. Instead of
824 gabazine, 10 µM CNO were bath-applied after the baseline recording of IPSCs. Measures of

825 charge transfer were used to take into account the variable waveform of the IPSCs that were
826 composed of multiple superimposed burst-like synaptic events.

827 To determine the connectivity of PV- and Sst-expressing TRN cells, brain slices were prepared
828 from PV-Cre and Sst-Cre lines previously injected with ChR2-expressing virus (see above). Using
829 identical recording and light stimulation conditions, evoked IPSCs were quantified in neurons
830 recorded in the different thalamic nuclei AD, AV and LD.

831 ***In vivo* single-unit recordings and head-direction monitoring**

832 Electrode and fiber preparation.

833 Two types of recording configurations were used. Multi-wire electrodes were implanted for
834 studying response properties of ATN+ to PreS/RSC stimulation. Silicon probes were used for
835 identification and recording of AD HD-tuned units in combination with optogenetic activation of
836 PreS/RSC and/or chemogenetic silencing of the anterodorsal TRN.

837 Three mice were implanted with the multi-wire electrodes that consisted of 16 individually
838 insulated nichrome wires (13-µm inner diameter, impedance 1 – 3 MΩ; California Fine Wire)
839 contained in a 26-gauge stainless steel guide canula. The wires were attached to a 16-pin
840 connector (CON/16m-V-t, Omnetics) (Courtin et al., 2014), cut at a length of ~2 mm from the edge
841 of the metal guiding tube and gold-plated using a nanoZ™ device (White Matter LLC, provided by
842 Plexon Inc., Dallas, TX) to a final impedance of 50 – 100 kΩ. A silver wire (Warner Instr.) was
843 soldered to the ground pin of the connector. Six mice were implanted with a single shank linear
844 silicone probe (Neuronexus A1x16-5mm-50-703-Z16 or A1x16-3mm-50-703-Z16).

845 The optic fibers were built from a standard hard cladding multimode fiber (225 µm outer diameter,
846 Thorlabs, BFL37-2000/FT200EMT), inserted and glued (Heat-curable epoxy, Precision Fiber
847 Products, ET-353ND-16OZ) to a multimode ceramic zirconia ferrule (Precision Fiber Products,
848 MM-FER2007C-2300). The penetrating end was cut at the desired length (~2 mm) with a Carbide-
849 tip fiber optic scribe (Precision Fiber Products, M1-46124). The other end was polished with fiber-
850 polishing films (Thorlabs). The optic fibers were connected to a PlexBright Optogenetic
851 Stimulation System (Plexon) via home-made patch chord. The connection to the PlexBright Table-
852 top LED Module (Wavelength 465 nm) was achieved through a Mini MM FC 900µm Connector
853 (Precision Fiber Products, MM-CON2004-2300-14-BLK). The other end of the patch chord was
854 inserted into a ceramic zirconia ferrule, fixed with glue and heat-shrinking tube (Allied Electronics,

855 689-0267) and polished. Before the recording, the patch chord was attached to the implanted
856 optic fiber via a ceramic split sleeve (Precision Fiber Products, SM-CS125S).

857 Surgery.

858 Virally injected C57BL6/J and VGAT-Ires-Cre mice were anesthetized with 5 % isoflurane, fixed
859 on a stereotaxic frame and kept on a feedback-controlled heating pad (Phymep). The level of
860 isoflurane was reduced along the surgery until 1 % and mixed with N_2O. Craniotomies were
861 opened above the PreS (AP, ML, DV: -3.8, +/-2.5, -1.7 for vertical implantation, -3.8, -3.0, -1.5
862 with a 30° angle for implantation in diagonal), the left ATN for multi-wire electrodes (AP, ML, DV:
863 -0.8, +0.75, -2.8) or left AD for silicone probes (AP, ML, DV: -0.8, +0.75, -3.3) and the lateral
864 cerebellum with a microdrill (1/005 drill-size). The conjunctive tissue on the skull was removed
865 with a scalpel and the skull was cleaned with iodine-based disinfectant. The skull was then
866 scratched with the tip of the scalpel in a grid-like meshwork of grooves to improve the attachment
867 of the glue (Loctite 401, Koening). Multi-wire electrodes and linear silicone probes were lowered
868 vertically, at approximately 10 µm/s initially and then 1 µm/s when reaching the ATN+/AD and
869 glued to the skull. Optic fibers were lowered vertically or in diagonal above the PreS at similar
870 rates. For the multi-wire electrodes, the ground silver wire was implanted at the surface of the
871 lateral cerebellum. For silicone probes, the external reference and ground wires were twisted
872 together and implanted at the surface of the lateral cerebellum. Carprofen (5 mg/kg, i.p.) and
873 paracetamol (2 mg/mL, drinking water) were provided during the peri-operative period. The mice
874 were left in their home cage for a week to recover from the surgery and their weight, behavior and
875 all aspects were monitored in score sheets established with the veterinary protocols. During this
876 period, mice were also habituated to the handling and the recording cables.

877 Unit recordings and HD monitoring.

878 Mice were placed into a large cylindrical Plexiglas cage (diameter: 50 cm, height: 40 cm) where
879 they could freely behave all along the recording sessions. The cage was positioned below a vision
880 color camera inside a Faraday cage. Implanted animals were connected to the pre-amplifier PZ5-
881 32 (Tucker-Davis Technologies (TDT)) via a ZIF-Clip Headstage adaptor (TDT, ZCA-OMN16) for
882 the multi-wire electrodes and a ZIF-Clip Headstage (TDT) for the silicone probes. The camera
883 was connected to a RV2 collection device (TDT) capable of tracking red and green LEDs mounted
884 on the ZIF-Clip Headstage. The preamplifier was connected to a main amplifier RZ5D (TDT). The
885 main computer (WS8, TDT) used the Real-time Processor Visual Design Studio (RPvdsEx) tool
886 to design the recording sessions, activate light stimulation from the PlexBright Optogenetic

887 Stimulation System (Plexon), and acquire the electrophysiological data from the headstage and
888 tracking data from the camera.

889 For optogenetic stimulation of the PreS/RSC (in 3 multiwire-implanted and 4 silicone probe-
890 implanted mice), a recording session consisted in a 10 – 20 min baseline recording followed by a
891 10 – 20 min recording with optogenetic activation of the PreS/RSC. The stimulation consisted in
892 300 – 600 light stimulations of 10 ms duration, one stimulation every 2 s. The intensity of the light
893 ranged from 2 – 6 mW depending on the quality of the homemade optic fibers. For chemogenetic
894 silencing of the anterodorsal TRN (in 5 silicone probe-implanted mice), a recording session
895 consisted in a 10 – 20 min baseline recording, i.p. injection of CNO (1 – 2 mg/kg) or NaCl, 40 min
896 resting in homecage and 10 – 20 min test recording. The timing of the CNO injection is based on
897 previous *in vivo* work using the same mouse line and CNO products, showing that the CNO effect
898 peaked ~30 min post i.p. injection (Fernandez et al., 2018). For the combination of both
899 optogenetic activation of PreS/RSC and chemogenetic silencing of the anterodorsal TRN (in 3
900 silicone probe-implanted mice), the recording sessions consisted of 10 min baseline, 10 min
901 optogenetic stimulation, i.p. injection of CNO (1 – 2 mg/kg), 40 min resting in homecage, 10 min
902 second baseline and 10 min optogenetic stimulation. The number of recording sessions per
903 mouse ranged from 1-3.

904 <u>Spike sorting.</u>

905 The Offline Sorter software (Plexon), Neuroexplorer (Nex Technologies) and MATLAB
906 (MathWorks) were used to sort and analyze single-unit spikes. The waveforms were manually
907 delineated in the two-dimensional space of principal components using their voltage features.
908 Single units were defined as discrete clusters of waveforms in the principal component space,
909 and did not contain spikes with a refractory period less than 1 ms. The quantification of the clusters
910 separation was further measured with multivariate ANOVA and J3 statistics. Cross-correlation
911 analyses were used to control that a single unit was not recorded on multiple channels. Target
912 units that had a peak of spike discharge when the reference unit fired were considered as
913 duplicates and only one of the copy was used for analysis (Adapted from (Rozeske et al., 2018)).
914 To compare the recordings during baseline and after injection of CNO or NaCl, units were sorted
915 with two different methods. At first, both recording sessions were manually sorted as described
916 above while the experimenter was blind to the baseline and CNO/NaCl condition. In a second
917 step, the baseline sorting template was used for the CNO/NaCl recording. Both methods gave
918 similar results and only the manual sorted data are shown. Some units were stable across
919 sessions over several days or weeks, as evident by their identical firing rate, preferred direction

920 and their detection on the same recording channel. In such cases with duplicates, only the first
921 recording session was kept. Results did not change when analysis of later sessions were used.

922 Unit analysis.

923 The discharge pattern of well-defined single units in the ATN+ was aligned to the optogenetic
924 stimulation using peri-event raster plots and cumulative histogram (5 ms bins, starting 50 ms
925 before LED onset and lasting 200 ms after LED onset, Neuroexplorer). The firing rate 50 ms
926 before the LED onset was used as a baseline to calculate the z-score of each bin as follows: =
927 $\frac{measured\ valued - baseline\ average}{baseline\ standard\ error}$. Z-scores were considered significant when > 1.96 and < -1.96.
928 Significant changes in the firing rate fell into 4 distinct classes depending on the direction of the
929 change (increase or decrease firing) and the timing of the change. The latencies were measured
930 from LED onset to the first bin showing a significant z-score value. In Fig. 5K, the averaged z-
931 score was measured from the first significant bin to the last significant bin. This range included
932 sometimes bins that were below significance and were sparsely distributed within the evoked
933 event. The range of bins included to quantify decrease or early increase in firing rate was identical
934 for the baseline and the CNO recordings and based on the earliest and last significant bin
935 regardless of the condition.

936 Using a custom-made Matlab routine, the discharge patterns of ATN+ units were binned to the
937 HD of the mice. The angles of direction were binned in 6°. The firing rate was averaged for each
938 of the 60 portions of the circle. The length of the Rayleigh vector (r) was calculated and units were
939 considered as HD if $r \geq 0.4$, as head-modulated if $0.2 \leq r < 0.4$ and as not tuned if $r < 0.2$ (Yoder
940 and Taube, 2009). The maximal firing rate, the width and the preferred direction were calculated
941 for HD units. The width of the tuning curve was measured as the span of the angle between the
942 two directions for which the firing rate was equal to 50 % of the maximal firing rate at the preferred
943 direction (Blair and Sharp, 1995).

944

945 **Behavioral experiment**

946 Recording.

947 One week before the beginning of the behavioral task, VGAT-Ires-Cre mice expressing either an
948 hM4D or a non-hM4D -related (control mice) construct into the anterodorsal TRN were habituated
949 to the handling and i.p. injection. Naïve VGAT-Ires-Cre male mice were trained to find a 12 cm
950 wide circular platform submerged 0.5 – 0.8 cm below the surface in a 150 cm diameter circular

951 pool filled with white opaque water at 23±1°C. Mice were trained in daily sessions composed of 4
952 consecutive trials, with a 60 s probe session without the platform preceding the first trial session
953 every odd days. A trial ended when the mice spent 5 s onto the platform. Mice were left 10 s more
954 before being placed below a heating lamp before the next trial, 10 – 15 s later. Four shapes
955 around the pool (cross, horizontal stripes, vertical stripes, coffee grain) served as visual cues and
956 were placed in the SW, NW, NE, SE corner of the room respectively. If the mouse failed to find
957 the platform after 60 s, the experimenter guided it to the platform where it was left for 15 s. Mice
958 were placed in the pool facing the wall. The position of pool entry was randomly shuffled every
959 day between NE, SE, NW and NE. During a 60 s probe session, the platform was removed and
960 mice were released from the wall of the quadrant opposite to the target one. The experimenter
961 was blind to the condition of the mice (control or hM4D). The session duration (between the first
962 and the last animal) was ~2 hours, the first trial starting at Zeitgeber time 0 + 1.5 h. Daily i.p.
963 injection of CNO (1 – 2 mg/kg) were performed 40 min before the beginning of the session. The
964 timing of the CNO injection is based on previous *in vivo* work using the same mouse line and
965 CNO products, showing that the CNO effect peaked ~30 min post i.p. injection (Fernandez et al.,
966 2018).

967 Analysis and automatic strategy detection.

968 The video tracking data were analyzed using EthoVisionXT14 (Noldus) to quantify the average
969 swimming speed, escape latency, proximity (mean distance of all the tracked points of the path
970 to the platform center), percentage time spent in target quadrant and platform crossings.
971 Heatmaps were generated by superimposing all the path points of every mouse in a group.
972 Heatmaps were linearly scaled using the global minimum and maximum for both groups to allow
973 comparison between the two. To attribute a specific strategy to each MWM trial, we used a
974 homemade matlab algorithm based on (Garthe et al., 2009). For each trial, the animal path in the
975 MWM was extracted as timed-tagged x and y coordinates from which specific variables were
976 computed in order to take a decision. The 8 strategies are described in Suppl. Fig. 5 and the
977 decision was made in the following sequential order with the 4 allocentric strategies first followed
978 by the 4 egocentric strategies: 1-Direct swimming; if 95 % of the time-points are spent in the goal
979 cone (isosceles triangle with its height going from starting point to goal platform with an origin
980 angle of 40°). 2-Focal search; if the mean distance of the path to its centroid (MDTC) was inferior
981 to 35 % standard unit (STDU) corresponding to the radius of the MWM, and the mean distance
982 to the edge of the goal platform was inferior to 30% STDU. 3-directed search; if total time spent
983 in the goal cone was superior to 80 %. 4-perseverance; if the MDTC was inferior to 45 % STDU

984 and the mean distance to the previous platform edge was inferior to 40 % STDU. In our case, the
985 perseverance strategy was only possible after day 10, during the reversal learning period. 5-
986 chaining; if the time spent in the annulus zone (spanning from 33 to 70 % STDU) was superior to
987 80 %. 6-scanning; if the total coverage of the MWM (the pool was divided in 15 cm squares and
988 the coverage was obtained as the ratio of crossed squares over the total number of squares) was
989 superior to 10% and inferior to 60 %, and the mean distance of the path to the center of the MWM
990 was inferior to 70% STDU. 7-thigmotaxis; if the time spent in the closer wall zone (spanning from
991 87 % STDU to the edge of the MWM) was superior to 35 % and the time spend in the wider wall
992 zone (spanning from 70 % STDU to the edge of the MWM) was superior to 65 %. 8-random
993 search; if the total coverage of the MWM was superior to 60 %. If none the conditions could be
994 met in this order, no strategy were attributed.

995 Histology

996 At the end of the recording sessions, mice were perfused as described in the previous section:
997 Perfusion and tissue processing. Brain sections were directly mounted on slides and observed
998 though a fluorescent stereomicroscope (Nikon SMZ 25) and NIS-Elements 4.5 (Nikon) was used
999 to analyse images. Mice showing expression of the hM4D construct outside of the anterior sector
1000 of the TRN or only were excluded.
1001

1002 **Statistics**

1003 All tests were done using R programming software (2.15.0, R Core Team, The R Foundation for
1004 Statistical Computing (www.rproject.org/foundation), 2007]. The normality of the data sets was
1005 assessed using Shapiro-Wilk normality test. Comparison of two data sets were done using
1006 Student's *t* test and paired Student's *t* test, for non-repeated and repeated measures respectively,
1007 or their non-parametric equivalent, Mann-Whitney U test and Wilcoxon signed rank-test. Chi-
1008 square tests were used to assess whether the swimming region of mice during probe sessions of
1009 the MWM were different from the expected frequencies and the proportion of strategies used
1010 between mouse groups. 1-way/2-way (non-)repeated measure ANOVAs followed by post hoc *t*
1011 tests were used when necessary on normally distributed data sets whereas non-normally
1012 distributed data were analyzed directly with the post hoc tests. A Bonferroni correction was
1013 applied when more than two comparisons were done on the same data set and the new alpha
1014 threshold is indicated. All statistical tests are specifically indicated in the figure legends if they are
1015 not given in the main text.

1016 **References**

1017 Ahrens, S., Jaramillo, S., Yu, K., Ghosh, S., Hwang, G.R., Paik, R., Lai, C., He, M., Huang, Z.J.,
1018 and Li, B. (2015). ErbB4 regulation of a thalamic reticular nucleus circuit for sensory selection.
1019 Nat. Neurosci. *18*, 104-111.
1020 Astori, S., and Lüthi, A. (2013). Synaptic plasticity at intrathalamic connections via $Ca_V3.3$ T-type
1021 Ca^{2+} channels and GluN2B-containing NMDA receptors. J. Neurosci. *33*, 624-630.
1022 Awasthi, A., Ramachandran, B., Ahmed, S., Benito, E., Shinoda, Y., Nitzan, N., Heukamp, A.,
1023 Rannio, S., Martens, H., Barth, J.*, et al.* (2019). Synaptotagmin-3 drives AMPA receptor
1024 endocytosis, depression of synapse strength, and forgetting. Science *363*, eaav1483.
1025 Blair, H.T., Cho, J., and Sharp, P.E. (1998). Role of the lateral mammillary nucleus in the rat head
1026 direction circuit: a combined single unit recording and lesion study. Neuron *21*, 1387-1397.
1027 Blair, H.T., and Sharp, P.E. (1995). Anticipatory head direction signals in anterior thalamus:
1028 evidence for a thalamocortical circuit that integrates angular head motion to compute head
1029 direction. J. Neurosci. *15*, 6260-6270.
1030 Bubb, E.J., Kinnavane, L., and Aggleton, J.P. (2017). Hippocampal - diencephalic - cingulate
1031 networks for memory and emotion: An anatomical guide. Brain Neurosci. Adv. *1*, 1-20.
1032 Butler, W.N., Smith, K.S., van der Meer, M.A.A., and Taube, J.S. (2017). The head-direction
1033 signal plays a functional role as a neural compass during navigation. Curr. Biol. *27*, 1259-1267.
1034 Calton, J.L., and Taube, J.S. (2005). Degradation of head direction cell activity during inverted
1035 locomotion. J. Neurosci. *25*, 2420-2428.
1036 Castro-Alamancos, M.A., and Calcagnotto, M.E. (1999). Presynaptic long-term potentiation in
1037 corticothalamic synapses. J. Neurosci. *19*, 9090-9097.
1038 Clark, B.J., Bassett, J.P., Wang, S.S., and Taube, J.S. (2010). Impaired head direction cell
1039 representation in the anterodorsal thalamus after lesions of the retrosplenial cortex. J. Neurosci.
1040 *30*, 5289-5302.
1041 Clark, B.J., Simmons, C.M., Berkowitz, L.E., and Wilber, A.A. (2018). The retrosplenial-parietal
1042 network and reference frame coordination for spatial navigation. Behav. Neurosci. *132*, 416-429.
1043 Clemente-Perez, A., Makinson, S.R., Higashikubo, B., Brovarney, S., Cho, F.S., Urry, A., Holden,
1044 S.S., Wimer, M., David, C., Fenno, L.E.*, et al.* (2017). Distinct thalamic reticular cell types
1045 differentially modulate normal and pathological cortical rhythms. Cell Rep. *19*, 2130-2142.
1046 Cornwall, J., Cooper, J.D., and Phillipson, O.T. (1990). Projections to the rostral reticular thalamic
1047 nucleus in the rat. Exp. Brain Res. *80*, 157-171.
1048 Courtin, J., Chaudun, F., Rozeske, R.R., Karalis, N., Gonzalez-Campo, C., Wurtz, H., Abdi, A.,
1049 Baufreton, J., Bienvenu, T.C., and Herry, C. (2014). Prefrontal parvalbumin interneurons shape
1050 neuronal activity to drive fear expression. Nature *505*, 92-96.
1051 Crabtree, J.W. (2018). Functional diversity of thalamic reticular subnetworks. Front. Syst.
1052 Neurosci. *12*, 41.
1053 Crandall, S.R., Cruikshank, S.J., and Connors, B.W. (2015). A corticothalamic switch: controlling
1054 the thalamus with dynamic synapses. Neuron *86*, 768-782.
1055 Cruikshank, S.J., Urabe, H., Nurmikko, A.V., and Connors, B.W. (2010). Pathway-specific
1056 feedforward circuits between thalamus and neocortex revealed by selective optical stimulation of
1057 axons. Neuron *65*, 230-245.
1058 Ding, S.L. (2013). Comparative anatomy of the prosubiculum, subiculum, presubiculum,
1059 postsubiculum, and parasubiculum in human, monkey, and rodent. J. Comp. Neurol. *521*, 4145-
1060 4162.
1061 Dolleman-van der Weel, M.J., Morris, R.G., and Witter, M.P. (2009). Neurotoxic lesions of the
1062 thalamic reuniens or mediodorsal nucleus in rats affect non-mnemonic aspects of watermaze
1063 learning. Brain Struct. Funct. *213*, 329-342.

1064 Dong, P., Wang, H., Shen, X.F., Jiang, P., Zhu, X.T., Li, Y., Gao, J.H., Lin, S., Huang, Y., He,
1065 X.B., *et al.* (2019). A novel cortico-intrathalamic circuit for flight behavior. Nat. Neurosci. *22*, 941-
1066 949.
1067 Dumont, J.R., and Taube, J.S. (2015). The neural correlates of navigation beyond the
1068 hippocampus. Prog. Brain Res. *219*, 83-102.
1069 Duszkiewicz, A.J., Brown, E., Wood, E.R., and Peyrache, A. (2019). Thalamic reticular nucleus
1070 controls the gain of the thalamic head-direction signal. Program No. 604.618. 2019 Neuroscience
1071 Meeting Planner. Chicago, IL: Society for Neuroscience, 2019. Online.
1072 Fernandez, L.M.J., Pellegrini, C., Vantomme, G., Béard, E., Lüthi, A., and Astori, S. (2017).
1073 Cortical afferents onto the nucleus Reticularis thalami promote plasticity of low-threshold
1074 excitability through GluN2C-NMDARs. Sci. Rep. *7*, 12271.
1075 Fernandez, L.M.J., Vantomme, G., Osorio-Forero, A., Cardis, R., Béard, E., and Lüthi, A. (2018).
1076 Thalamic reticular control of local sleep in mouse sensory cortex. Elife *7*, e39111.
1077 Garthe, A., and Kempermann, G. (2013). An old test for new neurons: refining the Morris water
1078 maze to study the functional relevance of adult hippocampal neurogenesis. Front. Neurosci. *7*,
1079 63.
1080 Gentet, L.J., and Ulrich, D. (2004). Electrophysiological characterization of synaptic connections
1081 between layer VI cortical cells and neurons of the nucleus reticularis thalami in juvenile rats. Eur.
1082 J. Neurosci. *19*, 625-633.
1083 Gjoni, E., Zenke, F., Bouhours, B., and Schneggenburger, R. (2018). Specific synaptic input
1084 strengths determine the computational properties of excitation-inhibition integration in a sound
1085 localization circuit. J. Physiol. *596*, 4945-4967.
1086 Golshani, P., Liu, X.B., and Jones, E.G. (2001). Differences in quantal amplitude reflect GluR4-
1087 subunit number at corticothalamic synapses on two populations of thalamic neurons. Proc. Natl.
1088 Acad. Sci. USA *98*, 4172-4177.
1089 Gonzalo-Ruiz, A., and Lieberman, A.R. (1995a). GABAergic projections from the thalamic
1090 reticular nucleus to the anteroventral and anterodorsal thalamic nuclei of the rat. J. Chem.
1091 Neuroanat. *9*, 165-174.
1092 Gonzalo-Ruiz, A., and Lieberman, A.R. (1995b). Topographic organization of projections from the
1093 thalamic reticular nucleus to the anterior thalamic nuclei in the rat. Brain Res. Bull. *37*, 17-35.
1094 Goodridge, J.P., and Taube, J.S. (1997). Interaction between the postsubiculum and anterior
1095 thalamus in the generation of head direction cell activity. J. Neurosci. *17*, 9315-9330.
1096 Halassa, M.M., Chen, Z., Wimmer, R.D., Brunetti, P.M., Zhao, S., Zikopoulos, B., Wang, F.,
1097 Brown, E.N., and Wilson, M.A. (2014). State-dependent architecture of thalamic reticular
1098 subnetworks. Cell *158*, 808-821.
1099 Herrera, C.G., Cadavieco, M.C., Jego, S., Ponomarenko, A., Korotkova, T., and Adamantidis, A.
1100 (2016). Hypothalamic feed-forward inhibition of thalamocortical network controls arousal and
1101 consciousness. Nat. Neurosci. *19*, 290-298.
1102 Hinman, J.R., Dannenberg, H., Alexander, A.S., and Hasselmo, M.E. (2018). Neural mechanisms
1103 of navigation involving interactions of cortical and subcortical structures. J. Neurophysiol. *119*,
1104 2007-2029.
1105 Huguenard, J.R. (1996). Low-threshold calcium currents in central nervous system neurons.
1106 Annu. Rev. Physiol. *58*, 329-348.
1107 Knudsen, E.I. (2018). Neural Circuits That Mediate Selective Attention: A Comparative
1108 Perspective. Trends Neurosci. *41*, 789-805.
1109 Krol, A., Wimmer, R.D., Halassa, M.M., and Feng, G. (2018). Thalamic reticular dysfunction as a
1110 circuit endophenotype in neurodevelopmental disorders. Neuron *98*, 282-295.
1111 Krout, K.E., Loewy, A.D., Westby, G.W., and Redgrave, P. (2001). Superior colliculus projections
1112 to midline and intralaminar thalamic nuclei of the rat. J. Comp. Neurol. *431*, 198-216.
1113 Le Masson, G., Renaud-Le Masson, S., Debay, D., and Bal, T. (2002). Feedback inhibition
1114 controls spike transfer in hybrid thalamic circuits. Nature *417*, 854-858.

Lee, S.M., Friedberg, M.H., and Ebner, F.F. (1994). The role of GABA-mediated inhibition in the rat ventral posterior medial thalamus. II. Differential effects of $GABA_A$ and $GABA_B$ receptor antagonists on responses of VPM neurons. J. Neurophysiol. *71*, 1716-1726.

Lozsádi, D.A. (1994). Organization of cortical afferents to the rostral, limbic sector of the rat thalamic reticular nucleus. J. Comp. Neurol. *341*, 520-533.

Lozsádi, D.A. (1995). Organization of connections between the thalamic reticular and the anterior thalamic nuclei in the rat. J. Comp. Neurol. *358*, 233-246.

Miniaci, M.C., and De Leonibus, E. (2018). Missing the egocentric spatial reference: a blank on the map. F1000Res *7*, 168.

Mitchell, A.S., Czajkowski, R., Zhang, N., Jeffery, K., and Nelson, A.J.D. (2018). Retrosplenial cortex and its role in spatial cognition. Brain Neurosci. Adv. *2*, 1-13.

Paré, D., Steriade, M., Deschênes, M., and Oakson, G. (1987). Physiological characteristics of anterior thalamic nuclei, a group devoid of inputs from reticular thalamic nucleus. J. Neurophysiol. *57*, 1669-1685.

Perry, B.A.L., and Mitchell, A.S. (2019). Considering the evidence for anterior and laterodorsal thalamic nuclei as higher order relays to cortex. Front. Mol. Neurosci. *12*, 167.

Peyrache, A., Duszkiewicz, A.J., Viejo, G., and Angeles-Duran, S. (2019). Thalamocortical processing of the head-direction sense. Prog. Neurobiol. *183*, 101693.

Peyrache, A., Lacroix, M.M., Petersen, P.C., and Buzsáki, G. (2015). Internally organized mechanisms of the head direction sense. Nat. Neurosci. *18*, 569-575.

Peyrache, A., Schieferstein, N., and Buzsáki, G. (2017). Transformation of the head-direction signal into a spatial code. Nat. Commun. *8*, 1752.

Pinault, D. (2004). The thalamic reticular nucleus: structure, function and concept. Brain Res. Rev. *46*, 1-31.

Pinault, D., and Deschênes, M. (1998). Projection and innervation patterns of individual thalamic reticular axons in the thalamus of the adult rat: a three-dimensional, graphic, and morphometric analysis. J. Comp. Neurol. *391*, 180-203.

Rogers, J., Churilov, L., Hannan, A.J., and Renoir, T. (2017). Search strategy selection in the Morris water maze indicates allocentric map formation during learning that underpins spatial memory formation. Neurobiol. Learn. Mem. *139*, 37-49.

Rozeske, R.R., Jercog, D., Karalis, N., Chaudun, F., Khoder, S., Girard, D., Winke, N., and Herry, C. (2018). Prefrontal-periaqueductal gray-projecting neurons mediate context fear discrimination. Neuron *97*, 898-910.

Scheibel, M.E., and Scheibel, A.B. (1966). The organization of the nucleus reticularis thalami: a Golgi study. Brain Res. *1*, 43-62.

Sharp, P.E., Blair, H.T., and Cho, J. (2001a). The anatomical and computational basis of the rat head-direction cell signal. Trends Neurosci. *24*, 289-294.

Sharp, P.E., Tinkelman, A., and Cho, J. (2001b). Angular velocity and head direction signals recorded from the dorsal tegmental nucleus of gudden in the rat: implications for path integration in the head direction cell circuit. Behav. Neurosci. *115*, 571-588.

Sherman, S.M. (2017). Functioning of circuits connecting thalamus and cortex. Compr. Physiol. *7*, 713-739.

Sherman, S.M., and Guillery, R.W. (1998). On the actions that one nerve cell can have on another: distinguishing "drivers" from "modulators". Proc. Natl. Acad. Sci. USA *95*, 7121-7126.

Simonnet, J., and Fricker, D. (2018). Cellular components and circuitry of the presubiculum and its functional role in the head direction system. Cell Tissue Res. *373*, 541-556.

Soto-Sánchez, C., Wang, X., Vaingankar, V., Sommer, F.T., and Hirsch, J.A. (2017). Spatial scale of receptive fields in the visual sector of the cat thalamic reticular nucleus. Nat. Commun. *8*, 800.

Stackman, R.W., Jr., Lora, J.C., and Williams, S.B. (2012). Directional responding of C57BL/6J mice in the Morris water maze is influenced by visual and vestibular cues and is dependent on the anterior thalamic nuclei. J. Neurosci. *32*, 10211-10225.

1166 Stackman, R.W., and Taube, J.S. (1998). Firing properties of rat lateral mammillary single units:
1167 head direction, head pitch, and angular head velocity. J. Neurosci. *18*, 9020-9037.
1168 Taube, J.S. (1995). Head direction cells recorded in the anterior thalamic nuclei of freely moving
1169 rats. J. Neurosci. *15*, 70-86.
1170 Taube, J.S., Kesslak, J.P., and Cotman, C.W. (1992). Lesions of the rat postsubiculum impair
1171 performance on spatial tasks. Behav. Neural Biol. *57*, 131-143.
1172 Taube, J.S., Muller, R.U., and Ranck, J.B., Jr. (1990). Head-direction cells recorded from the
1173 postsubiculum in freely moving rats. I. Description and quantitative analysis. J. Neurosci. *10*, 420-
1174 435.
1175 Temereanca, S., and Simons, D.J. (2004). Functional topography of corticothalamic feedback
1176 enhances thalamic spatial response tuning in the somatosensory whisker/barrel system. Neuron
1177 *41*, 639-651.
1178 Tsanov, M., Chah, E., Vann, S.D., Reilly, R.B., Erichsen, J.T., Aggleton, J.P., and O'Mara, S.M.
1179 (2011). Theta-modulated head direction cells in the rat anterior thalamus. J. Neurosci. *31*, 9489-
1180 9502.
1181 Usrey, W.M., and Sherman, S.M. (2019). Corticofugal circuits: Communication lines from the
1182 cortex to the rest of the brain. J. Comp. Neurol. *527*, 640-650.
1183 Valerio, S., and Taube, J.S. (2012). Path integration: how the head direction signal maintains and
1184 corrects spatial orientation. Nat. Neurosci. *15*, 1445-1453.
1185 van der Meer, M.A.A., Richmond, Z., Braga, R.M., Wood, E.R., and Dudchenko, P.A. (2010).
1186 Evidence for the use of an internal sense of direction in homing. Behav. Neurosci. *124*, 164-169.
1187 van Groen, T., and Wyss, J.M. (1990). The postsubicular cortex in the rat: characterization of the
1188 fourth region of the subicular cortex and its connections. Brain Res. *529*, 165-177.
1189 Vantomme, G., Osorio-Forero, A., Lüthi, A., and Fernandez, L.M.J. (2019). Regulation of local
1190 sleep by the thalamic reticular nucleus. Front. Neurosci. *13*, 576.
1191 Vélez-Fort, M., Bracey, E.F., Keshavarzi, S., Rousseau, C.V., Cossell, L., Lenzi, S.C., Strom, M.,
1192 and Margrie, T.W. (2018). A circuit for integration of head- and visual-motion signals in layer 6 of
1193 mouse primary visual cortex. Neuron *98*, 179-191.
1194 Vong, L., Ye, C., Yang, Z., Choi, B., Chua, S., Jr., and Lowell, B.B. (2011). Leptin action on
1195 GABAergic neurons prevents obesity and reduces inhibitory tone to POMC neurons. Neuron *71*,
1196 142-154.
1197 Weese, G.D., Phillips, J.M., and Brown, V.J. (1999). Attentional orienting is impaired by unilateral
1198 lesions of the thalamic reticular nucleus in the rat. J. Neurosci. *19*, 10135-10139.
1199 Wilkins, L.K., Girard, T.A., Herdman, K.A., Christensen, B.K., King, J., Kiang, M., and Bohbot,
1200 V.D. (2017). Hippocampal activation and memory performance in schizophrenia depend on
1201 strategy use in a virtual maze. Psychiatry Res. Neuroimaging *268*, 1-8.
1202 Wimmer, R.D., Schmitt, L.I., Davidson, T.J., Nakajima, M., Deisseroth, K., and Halassa, M.M.
1203 (2015). Thalamic control of sensory selection in divided attention. Nature *526*, 705-709.
1204 Wright, N.F., Erichsen, J.T., Vann, S.D., O'Mara, S.M., and Aggleton, J.P. (2010). Parallel but
1205 separate inputs from limbic cortices to the mammillary bodies and anterior thalamic nuclei in the
1206 rat. J. Comp. Neurol. *518*, 2334-2354.
1207 Yoder, R.M., Peck, J.R., and Taube, J.S. (2015). Visual landmark information gains control of the
1208 head direction signal at the lateral mammillary nuclei. J. Neurosci. *35*, 1354-1367.
1209 Yoder, R.M., and Taube, J.S. (2009). Head direction cell activity in mice: robust directional signal
1210 depends on intact otolith organs. J. Neurosci. *29*, 1061-1076.
1211 Yoder, R.M., Valerio, S., Crego, A.C.G., Clark, B.J., and Taube, J.S. (2019). Bilateral
1212 postsubiculum lesions impair visual and nonvisual homing performance in rats. Behav. Neurosci.
1213 *133*, 496-507.
1214 Zikopoulos, B., and Barbas, H. (2007). Circuits formultisensory integration and attentional
1215 modulation through the prefrontal cortex and the thalamic reticular nucleus in primates. Rev.
1216 Neurosci. *18*, 417-438.

1217 Zikopoulos, B., and Barbas, H. (2012). Pathways for emotions and attention converge on the
1218 thalamic reticular nucleus in primates. J. Neurosci. *32*, 5338-5350.
1219 Zugaro, M.B., Arleo, A., Berthoz, A., and Wiener, S.I. (2003). Rapid spatial reorientation and head
1220 direction cells. J. Neurosci. *23*, 3478-3482.

1221